Journal of Alloys and Compounds 1000 (2024) 175025

Contents lists available at ScienceDirect

Journal of Alloys and Compounds

journal homepage: www.elsevier.com/locate/jalcom

Research article

Unusual superconductivity in crystallographically disordered $RT_{2-x}Sn_2$ compounds☆

Alessia Provino [a,b,c], Volodymyr Smetana [d], Vitalii Shtender [e], Stefanie Siebeneichler [d], Marina Putti [a,f], Alexandra Franz [g], Carlo Ferdeghini [a], Vitalij K. Pecharsky [c], Anja-Verena Mudring [d,h], Pietro Manfrinetti [a,b,c,*]

[a] Institute SPIN-CNR, Genova 16152, Italy
[b] Department of Chemistry, University of Genova, Genova 16146, Italy
[c] Ames Laboratory, US-DOE, Iowa State University, Ames, IA 50011-3020, USA
[d] Intelligent Advanced Materials, Department of Biological & Chemical Engineering and iNANO, Aarhus University, 8000 Aarhus C, Denmark
[e] Department of Chemistry - Ångström Laboratory, Uppsala University, Uppsala 75121, Sweden
[f] Department of Physics, University of Genova, Genova 16146, Italy
[g] Helmholtz-Zentrum Berlin, Berlin 14109, Germany
[h] Department of Physics, Umeå University, 901 87 Umeå, Sweden

ARTICLE INFO

Keywords:
Rare-earth ternary intermetallics
$RZn_{2-x}Sn_2$ compounds
Crystal structure
Superconductivity
Electronic structure
Rare earth stannides

ABSTRACT

The discovery of new superconducting materials represents a complementary and crucial tile to shed light on the mechanism controlling the phenomenon of superconductivity. During the search for new superconducting materials, we discovered a new series of intermetallic compounds with the general composition $RZn_{2-x}Sn_2$ (R = La, Ce, Pr, Nd). Their formation and crystal structure have been investigated. The Zn content decreases along the series from ≈ 1.50 in $LaZn_{1.50(1)}Sn_{1.98(2)}$ to ≈ 1.32 in $NdZn_{1.321(8)}Sn_{2.01(2)}$, due to the partial occupation of one of the two Zn sites [the Zn1 (2*c*) site, which from ≈ 50% in the La compound drops to ≈ 42%, ≈ 37% and ≈ 32% in the Ce, Pr and Nd compounds, respectively]. Both the Zn occupation factor and unit cell volume follow the lanthanide contraction. No such compound has been observed with Sm. AC and DC magnetic susceptibility and transport measurements revealed $LaZn_{1.5}Sn_2$ to undergo a sharp superconducting transition at T_c = 5.5 K. In order to search for further possible superconductive homologues, the lanthanum substituted phases $La(Zn,T)_{2-x}Sn_2$ (*T* = Ti, Mn, Fe, Co, Ni, Cu, Pd, Ag, Pt, Au, Cd; x ≈ 0.5) were also prepared. The crystal structure of the ternary compounds is a disordered defective derivative of the tetragonal $CaBe_2Ge_2$-type (*tP*10, *P*4/*nmm*), with a partially occupied Zn Wyckoff site and a disordered Sn position. Three related isostructural series, corresponding to three new prototypes, have been identified; they all contain conventional checkered pyramidal layers characteristic of the archetype. The magnetic and transport properties have been measured for some of these substituted quaternary La compounds and we found that superconductivity is preserved in them but in the orthorhombic compounds or when T was a magnetic transition metal (*e.g.*, Ni or Mn). A slight decrease in T_c down to about 4.0 K was detected as a result of the Zn by *T* atomic substitution.

1. Introduction

Superconductivity is a fascinating state of matter in which the electrical resistivity of a material drops to zero when the temperature is lowered below a critical value (T_c) [1]. Because the energy loss of the electric current flowing through a superconductor is extremely low, it can operate almost infinitely without any power supply and energy loss. This renders superconductors interesting for both fundamental science and technological applications, as they hold great promise in solving environmental and energy problems and addressing our global energy sustainability [2]. Aside from understanding the fundamentals of superconductivity [3], the most important research goal and dream for the scientific community is to find a superconductor operating at or close to ambient conditions. In this regard, the discovery of new

☆ Dedicated to the memory of Prof. Vitalij K. Pecharsky

* Corresponding author at: Department of Chemistry, University of Genova, Genova 16146, Italy.
E-mail address: pietro.manfrinetti@unige.it (P. Manfrinetti).

https://doi.org/10.1016/j.jallcom.2024.175025
Received 31 October 2023; Received in revised form 24 May 2024; Accepted 28 May 2024
Available online 29 May 2024

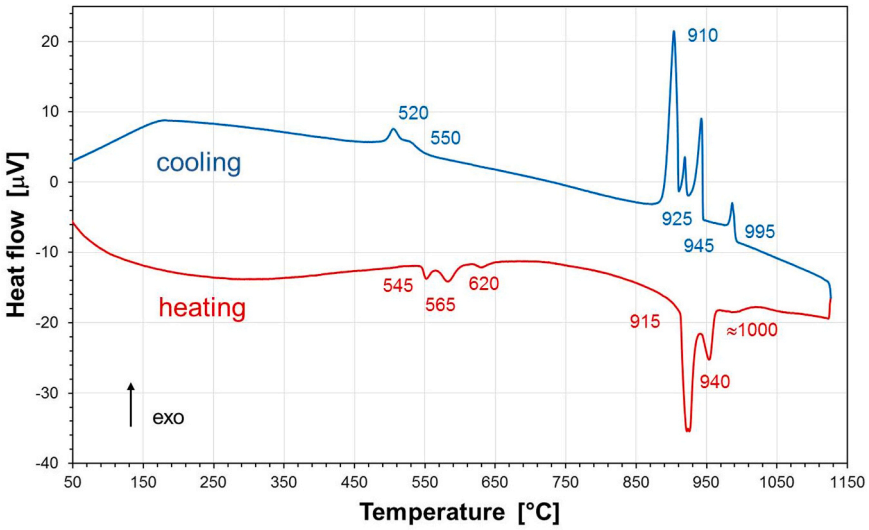

Fig. 1. DTA curves of a thermal cycle recorded at a rate of 10°C/min (both on heating and on cooling) for an almost single-phase sample with nominal composition $La_{22.2}Zn_{33.3}Sn_{44.5}$, previously annealed at 850°C (slowly cooled by shutting off the furnace). All given temperatures (data rounded to ± 2 units) are relative to the onset of the thermal effect (they are not peak temperature). The last weaker and broader thermal effect visible on heating happens around 1000°C.

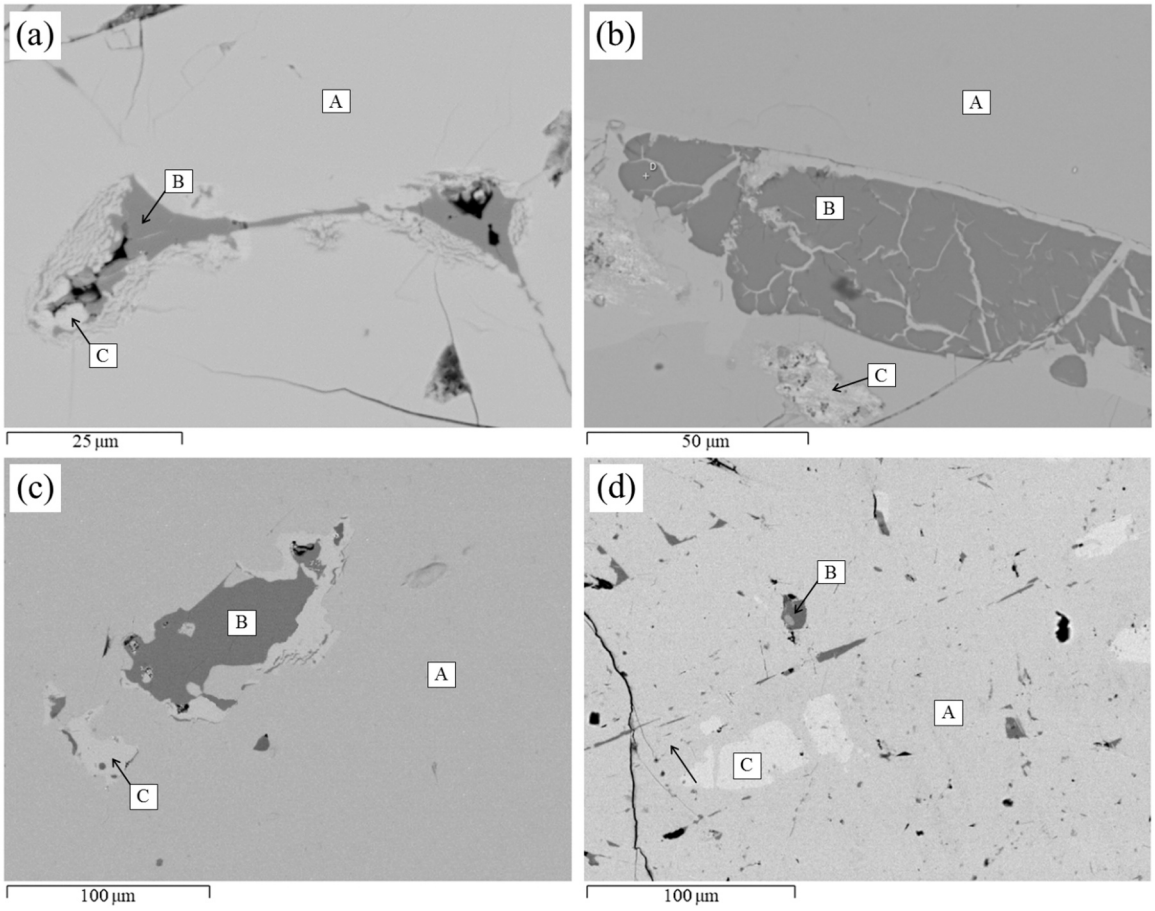

Fig. 2. SEM microphotographs [back scattered electron (BSE) mode] of the samples with nominal composition: $La_2Zn_3Sn_4$ (a), $Ce_2Zn_3Sn_4$ (b), $LaZn_{1.2}Cu_{0.4}Sn_2$ (c) and $LaZn_{1.2}Cd_{0.4}Sn_2$ (d). For each sample a region containing extra phases was magnified and EDX analyses performed to facilitate their identification. The large light-gray grains (indicated by A) belong to the $LaZn_{1.5}Sn_2$, $CeZn_{1.5}Sn_2$, $LaZn_{1.19}Cu_{0.39}Sn_{1.96}$ ($La_{22.0}Zn_{26.2}Cu_{8.6}Sn_{43.2}$) and $LaZn_{1.41}Cd_{0.15}Sn_{1.98}$ ($La_{22.0}Zn_{31.0}Cd_{3.4}Sn_{43.6}$) phases, respectively. The dark grains (indicated by B) are $LaZn_{13}$, $CeZn_{13}$, $LaZn_{13-x}Cu_x$ and $LaZn_{13-x-y}Cu_xCd_y$ phases. The trace amount of the light gray grains (indicated by C) are the binary/pseudobinary $LaSn_3$, $CeSn_3$, $La(Zn_xSn_{1-x})_3$ and $La(Zn_xCd_ySn_{1-x-y})_3$ phases [dissolving up to 7 and 3 at% Zn for $La(Zn_xSn_{1-x})_3$ and $La(Zn_xCd_ySn_{1-x-y})_3$, respectively] for the four samples, respectively.

Table 1
Single crystal data and refinement details for $RZn_{2-x}Sn_2$ (R = La, Pr, Nd) at T = 293 K.

Compound	$LaZn_{1.50(1)}Sn_{1.98(2)}$	$PrZn_{1.366(8)}Sn_{1.998(8)}$	$NdZn_{1.321(8)}Sn_{2.01(2)}$
Formula Weight [g/mol]	472.036	467.057	469.227
Structural prototype	defective $CaBe_2Ge_2$	defective $CaBe_2Ge_2$	defective $CaBe_2Ge_2$
Space group	*P4/nmm* (No. 129)	*P4/nmm* (No. 129)	*P4/nmm* (No. 129)
Pearson's symbol	*tP*10−x, x = 1.04	*tP*10−x, x = 1.278	*tP*10−x, x = 1.590
a [Å]	4.509(4)	4.435(2)	4.416(6)
c [Å]	10.67(1)	10.287(4)	10.24(2)
Unit cell volume [$Å^3$]	217.0(5)	202.3(2)	199.6(6)
Unit formula per cell, *Z*	2	2	2
Calculated density, ρ [g/cm^3]	7.221	7.666	7.790
Absorption coefficient, μ [mm^{-1}]	28.813	31.729	32.745
F(000)	402	399	399
Crystal description	Irregular fragment	Irregular fragment	Block
Crystal size [mm]	0.04 × 0.05 × 0.05	0.04 × 0.07 × 0.08	0.04 × 0.05 × 0.06
Theta range [°]	$3.819 \le \vartheta \le 29.971$	$3.962 \le \vartheta \le 33.249$	$5.028 \le \vartheta \le 31.900$
Index ranges *h*, *k*, *l*	$-4 \le h \le 6$ $-6 \le k \le 6$ $-15 \le l \le 15$	$-6 \le h \le 5$ $-6 \le k \le 6$ $-15 \le l \le 15$	$-5 \le h \le 4$ $-6 \le k \le 1$ $-14 \le l \le 9$
Reflections collected	1879	2444	588
Independent reflections	229	272	224
Absorption correction	Multi-scan	Multi-scan	Multi-scan
Refinement method	Full-matrix least-squares on F^2	Full-matrix least-squares on F^2	Full-matrix least-squares on F^2
Refined parameters	21	22	20
Data/restraints/parameter	229/0/21	272/0/22	224/0/20
Goodness of fit on F^2	1.431	1.285	1.162
$R1/wR^2$ (2σ)	0.0312/0.0734	0.0264/0.0587	0.0401/0.0892
$R1/wR^2$ (all data)	0.0380/0.0750	0.0337/0.0604	0.0563/0.0946
R_{int}	0.048	0.040	0.036
Largest diff. peak and hole [$e^-/Å^3$]	+2.281, −2.270	+1.190, −2.273	+1.531, −1.665

superconducting compounds irrespective of their T_c but with unique features represents a significant interest as it may lead to new classes of superconducting materials. This happened for the series of Fe-based superconductors, where starting from LaFePO, with a T_c of just 4 K [4], T_c as high as 56 K have been reached by doping through atomic substitutions [5]. While the BCS theory [1] successfully explains the behavior of low-temperature conventional superconductors characterized by weak electron-phonon interactions, it encounters limitations in explaining unconventional high–temperature superconductors due to the different mechanisms and more exotic interactions at play in these materials [6]. Nonetheless, it is worth noting that the BCS theory can offer insights into high-temperature superconductors such as hydrides.

Since the discovery of superconductivity, in 1911, many superconductors have been identified ranging from metals and intermetallic compounds to Fe-based materials, copper-based ceramics and pressurized molecular solids reaching, for these latter cases, very high T_c [7–9].

Intending to discover new materials with superconducting properties, we examined ternary systems formed by lanthanum, transition metals and *p*-block elements, particularly La-Zn-Sn. Although this system has been preliminary explored [10–12], the physical properties of the compounds have been barely examined [13]. Particularly, we were interested in a 1:2:2 phase adopting the crystal structure of one of the $BaAl_4$-type ordered derivatives [14]: $ThCr_2Si_2$ [15] or $CaBe_2Ge_2$ [16], the former being the representative prototype of the superconductors $Ba_{1-x}K_xFe_2As_2$ [17]. Despite numerous studies dedicated to finding novel superconductors within the $BaAl_4$ family, there are only a few examples of compounds crystallizing in the $CaBe_2Ge_2$-type showing superconducting behavior: $LaPd_2Pn_2$ (Pn = pnictide) [18,19], $SrPt_2As_2$ [20], $LaRh_2Ga_2$ [21] and $SrPd_2Bi_2$ [22]. While the 1:2:2 compounds have been reported with the other lanthanides Ce and Eu [23,24], preliminary screening of the La-Zn-Sn system [10] suggested the formation of a defect derivative phase having stoichiometry similar to $UCo_{1.5}Sn_2$ [25]; this latter being a subtype of the $CaBe_2Ge_2$ structure type. In our recent experiments, we found that $LaZn_{1.5}Sn_2$ is a superconductor and detected a T_c of 5.5 K [26]. This value of T_c is very close to that reported for the cubic high-temperature form of La metal (γ-La) [27,28].

In this work, we investigated the formation, crystal structure and exact composition of the $RZn_{2-x}Sn_2$ compounds for the light R (La-Nd) and several La substituted $La(Zn,T)_{2-x}Sn_2$ phases with T a transition metal [T = Ti, Mn, Fe, Co, Ni, Cu, Pd, Ag, Pt, Au and Cd ($x \approx 0.5$)]. As we were mainly interested in the La members, we will discuss the $RZn_{2-x}Sn_2$ compounds formed by other lanthanides only in light of structural details and compositional changes. For the $LaZn_{1.5}Sn_2$ and $LaZn_{1.2}Cu_{0.4}Sn_2$ compounds the magnetic and transport properties were also measured; the results will be discussed.

2. Experimental methods

2.1. Synthesis

Polycrystalline samples with nominal compositions RZn_2Sn_2 and $R_2Zn_3Sn_4$ (R = La, Ce, Pr, Nd and Sm), $LaZnCuSn_2$ and $LaZn_{1.2}T_{0.4}Sn_2$ (T = Ti, Mn, Fe, Co, Ni, Cu, Pd, Ag, Pt, Au, Cd) were prepared. The starting elements used were high-purity commercial metals (99.9 wt% for all R, 99.99 wt% for Zn and all transition metals, 99.999 wt% for Sn). To avoid any weight loss during the reaction (due to the high vapor pressure of Zn) the alloys were synthesized in sealed outgassed Ta crucible by high-frequency induction heating. Weighed amounts of the metals (in the form of freshly prepared turnings for R and of small pieces of all other metals) were pressed together directly into the Ta crucible, which was then sealed by arc welding under a pure-Ar flow. The total weight of the alloys was 2–5 g. The samples were melted by slowly heating the crucible up to 1200–1250°C (up to the liquid state of the alloys, but not too far above it to prevent possible breaking or explosion of the crucible), shaken to ensure homogenization and re-melted twice. A strong exothermic effect occurs during the first reaction of the metals. No contamination or reactivity of the samples towards the container material was noticed. The crucible was then sealed under vacuum in a fused silica tube, annealed at 800–900°C for 7–10 days (750°C the Sm sample) in a resistance furnace and finally air-cooled. The samples have metallic luster; when in pieces they are resistant to air for days, but in powder form are slightly air-sensitive.

Table 2
Single crystal data and refinement details for the tetragonal La(Zn,T)$_{2-x}$Sn$_2$ (T = Mn, Fe, Co, Ni, Cu, Pd, Pt) at T = 293 K.

Compound	$LaZn_{1.18}$ $_{(1)}Mn_{0.38}$ $_{(1)}Sn_{2.02(2)}$	$LaZn_{1.18}$ $_{(1)}Fe_{0.38}$ $_{(1)}Sn_{2.00(2)}$	$LaZn_{1.19}$ $_{(2)}Co_{0.33}$ $_{(3)}Sn_{1.993(4)}$	$LaZn_{1.18}$ $_{(1)}Ni_{0.38}$ $_{(1)}Sn_{1.98(2)}$	$LaZn_{1.18}$ $_{(1)}Cu_{0.38}$ $_{(1)}Sn_{2.00(2)}$ **(I)**	$LaZnCu_{0.764}$ $_{(3)}Sn_{2.000(2)}$ **(II)**	$LaZn_{1.11}$ $_{(1)}Pd_{0.44}$ $_{(2)}Sn_{2.01(2)}$	$LaZn_{1.05}$ $_{(1)}Pt_{0.50}$ $_{(2)}Sn_{2.03(2)}$
Formula Weight [g/mol]	476.778	474.745	472.757	473.442	477.641	490.265	497.501	546.216
Structural prototype	defective $CaBe_2Ge_2$	defective $CaBe_2Ge_2$	defective $CaBe_2Ge_2$	defective $CaBe_2Ge_2$	defective $CaBe_2Ge_2$	defective $CaBe_2Ge_2$	defective $CaBe_2Ge_2$	defective $CaBe_2Ge_2$
Space group	*P4/nmm* (No. 129)	*P4/nmm* (No. 129)	*P4/nmm* (No. 129)	*P4/nmm* (No. 129)	*P4/nmm* (No. 129)	*P4/nmm* (No. 129)	*P4/nmm* (No. 129)	*P4/nmm* (No. 129)
Pearson's symbol	*tP*10−x, x = 0.840	*tP*10−x, x = 0.876	*tP*10−x, x = 0.974	*tP*10−x, x = 0.912	*tP*10−x, x = 0.880	*tP*10−x, x = 0.418	*tP*10−x, x = 0.888	*tP*10−x, x = 0.832
a [Å]	4.4924(4)	4.4788(6)	4.4987(1)	4.485(2)	4.484(2)	4.4856(3)	4.509(2)	4.5169(2)
c [Å]	10.536(2)	10.542(2)	10.3961(5)	10.465(6)	10.592(5)	10.6178(6)	10.556(8)	10.4941(7)
Unit cell volume [Å^3]	212.63(5)	211.48(7)	210.40(1)	210.5(2)	212.9(2)	213.64(3)	214.6(2)	214.10(2)
Unit formula per cell, *Z*	2	2	2	2	2	2	2	2
Calculated density, ρ [g/cm^3]	7.448	7.467	7.461	7.484	7.426	7.646	7.676	8.476
Absorption coefficient, μ [mm^{-1}]	28.993	29.233	29.337	29.601	29.473	30.493	28.992	43.255
F(000)	406	405	402	405	406	420	421	458
Crystal description	Irregular fragment	irregular fragment	irregular fragment	Irregular fragment	Block	Irregular fragment	Irregular fragment	Irregular fragment
Crystal size [mm]	0.08 × 0.05 × 0.02	0.07 × 0.06 × 0.06	0.09 × 0.07 × 0.06	0.06 × 0.06 × 0.06	0.07 × 0.04 × 0.04	0.08 × 0.04 × 0.02	0.09 × 0.07 × 0.07	0.08 × 0.07 × 0.07
Theta range [°]	1.933 ≤ ϑ ≤ 29.982	1.932 ≤ ϑ ≤ 31.553	1.959 ≤ ϑ ≤ 32.855	3.894 ≤ ϑ ≤ 29.844	3.848 ≤ ϑ ≤ 29.952	3.838 ≤ ϑ ≤ 30.556	1.929 ≤ ϑ ≤ 29.972	1.941 ≤ ϑ ≤ 29.968
Index ranges *h*, *k*, *l*	−6 ≤ *h* ≤ 6 −6 ≤ *k* ≤ 3 −14 ≤ *l* ≤ 14	−5 ≤ *h* ≤ 6 −6 ≤ *k* ≤ 6 −15 ≤ *l* ≤ 15	−6 ≤ *h* ≤ 6 −6 ≤ *k* ≤ 6 −15 ≤ *l* ≤ 15	−6 ≤ *h* ≤ 5 −6 ≤ *k* ≤ 6 −14 ≤ *l* ≤ 14	−5 ≤ *h* ≤ 6 −6 ≤ *k* ≤ 6 −14 ≤ *l* ≤ 14	−6 ≤ *h* ≤ 6 −6 ≤ *k* ≤ 5 −14 ≤ *l* ≤ 15	−6 ≤ *h* ≤ 6 −6 ≤ *k* ≤ 5 −14 ≤ *l* ≤ 14	−6 ≤ *h* ≤ 6 −5 ≤ *k* ≤ 6 −14 ≤ *l* ≤ 14
Reflections collected	4168	5019	6060	3509	2196	2042	2836	2386
Independent reflections	224	253	269	218	223	237	221	218
Absorption correction	Multi-scan	Multi-scan	Multi-scan	Multi-scan	Multi-scan	Multi-scan	Multi-scan	Multi-scan
Refinement method	Full-matrix least-squares on F^2	Full-matrix least-squares on F^2	Full-matrix least-squares on F^2	Full-matrix least-squares on F^2	Full-matrix least-squares on F^2	Full-matrix least-squares on F^2	Full-matrix least-squares on F^2	Full-matrix least-squares on F^2
Refined parameters	21	21	25	21	21	17	27	27
Goodness of fit on F^2	1.219	1.179	1.072	1.128	1.171	1.121	1.183	1.181
$R1/wR^2$ (2σ)	0.0169/0.0371	0.0246/0.0649	0.0088/0.0136	0.0320/0.0612	0.0234/0.0661	0.0226/0.0562	0.0200/0.0414	0.0292/0.0617
$R1/wR^2$ (all data)	0.0232/0.0392	0.0301/0.0685	0.0108/0.0141	0.0443/0.0639	0.0250/0.0664	0.0237/0.0567	0.0210/0.0431	0.0297/0.0619
R_{int}	0.027	0.035	0.026	0.052	0.041	0.031	0.038	0.032
Largest diff. peak and hole [e$^-$/Å^3]	+1.225, −1.460	+2.151, −1.688	+0.503, −0.954	+1.513, −1.354	+1.849, −2.005	+1.386, −1.871	+0.869, −1.224	+2.017, −1.846

2.2. Phase analysis

Phase analysis was performed by both optical and scanning electron microscopy (OM and SEM), the latter equipped by energy-dispersive X-ray (EDX) microprobe for semi-quantitative analysis, and X-ray diffraction (XRD) investigation both on single crystal (SCXRD) and powder (PXRD). Micrographic specimens were prepared by standard polishing techniques. The microstructure, homogeneity and phase composition of the alloys were checked by a Leica Cambridge 360 microscope, equipped with an Oxford X-Max 20 analyzer (work parameters: EHT 20.0 kV and probe current 220 pA, counting time of 60 sec; Oxford Aztec software). The La(Zn$_x$Sn$_{1-x}$)$_3$ [or R(Zn$_x$Sn$_{1-x}$)$_3$] compound, present in the samples as an extra phase, was used as a standard for the R content; the precision of the measurements was estimated to be within 0.5 at%. X-ray powder patterns were recorded on a Guinier-Stoe camera [Cu-Kα1 radiation using pure Si as an internal standard; a = 5.4308(1) Å] and on a Philips diffractometer (Cu Kα radiation) for data collection (2θ range of 5°-105°, in steps of 0.02° and counting time of 24–26 s/step). The Guinier X-ray diffraction powder patterns were indexed with the help of Lazy Pulverix [29]. The full-profile Rietveld refinements were performed using the FULLPROF program [30].

2.3. Single crystal X-ray diffraction

Single crystals of the RZn$_{2-x}$Sn$_2$ (R = La, Pr and Nd), LaZn$_{1.2}$Cu$_{0.4}$Sn$_2$, and La(Zn,T)$_{2-x}$Sn$_2$ (T = Ti, Mn, Fe, Co, Ni, Cu, Pd, Ag, Cd, Pt, Au) samples were selected from a crushed fragment and affixed to a glass fiber with Apiezon C grease. They were tested at room temperature on either a Bruker APEX CCD diffractometer or a Bruker D8 VENTURE diffractometer (both with Mo Kα radiation; λ = 0.71073 Å), utilizing the APEX 2 and APEX 3 software suites (for the former and latter diffractometers, respectively) for data collection, integration, polarization, and empirical absorption correction [31]. Scans typically covered the θ range of ≈ 2–32°. The XPREP algorithms in the SHELXTL suite were used to check the intensity data sets for extinction conditions and E statistics necessary, allowing for the assignment of the proper space groups. Intrinsic phasing was used for the structure solutions (SHELXT) [32], while structure refinements (atomic position, site occupancy, and anisotropic displacement parameters) were carried out using SHELXL algorithms [33] within the APEX4 software. CCDC 2290618–2290629, 2298237 contain the supplementary crystallographic data for this paper. These data can be obtained free of charge via www.ccdc.cam.ac.uk/data_request/cif, or by emailing data_request@ccdc.cam.ac.uk, or

Table 3
Single crystal data and refinement details for the orthorhombic $LaZn_{1.446)}Sn_2$ (possible low-temperature form; see text) and the orthorhombic $La(Zn,T)_{2-x}Sn_2$ (T = Ti, Ag, Au, Cd) at T = 293 K.

Compound	$LaZn_{1.446(1)}Sn_{2.000(1)}$	$LaZn_{1.15(1)}Ti_{0.42(1)}Sn_{2.00(1)}$	$LaZn_{1.099(4)}Ag_{0.36(1)}Sn_{2.00(1)}$	$LaZn_{1.323(7)}Cd_{0.17(2)}Sn_{2.01(2)}$	$LaZn_{1.360(3)}Au_{0.269(7)}Sn_{2.01(2)}$
Formula Weight [g/mol]	478.879	471.628	487.022	483.608	519.427
Structural prototype	own	$LaZn_{1.1}Ag_{0.4}Sn_2$	own	$LaZn_{1.1}Ag_{0.4}Sn_2$	$LaZn_{1.1}Ag_{0.4}Sn_2$
Space group	*Cmmm* (No. 65)	*Cmmm* (No. 65)	*Cmmm* (No. 65)	*Cmmm* (No. 65)	*Cmmm* (No. 65)
Pearson's symbol	*oC*40−x, x = 4.436	*oC*108−x, x = 34.936	*oC*108−x, x = 36.644	*oC*108−x, x = 35.884	*oC*112−x, x =, x = 37.748
a [Å]	6.3181(8)	6.357(6)	6.4114(3)	6.369(1)	6.4108(3)
b [Å]	21.445(3)	42.16(4)	42.215(2)	42.492(9)	41.893(3)
c [Å]	6.3378(9)	6.337(6)	6.4023(3)	6.363(1)	6.3970(3)
Unit cell volume [$Å^3$]	858.7(2)	1699(3)	1732.8(1)	1722.0(5)	1718.0(2)
Unit formula per cell, *Z*	8	16	16	16	16
Calculated density, ρ [g/cm^3]	7.282	7.373	7.468	7.462	8.036
Absorption coefficient, μ [mm^{-1}]	28.962	28.372	28.417	29.116	37.699
F(000)	1603	3210	3311	3290	3514
Crystal description	Irregular fragment	Block	Irregular fragment	Irregular fragment	Irregular fragment
Crystal size [mm]	0.08 × 0.06 × 0.04	0.06 × 0.05 × 0.05	0.05 × 0.05 × 0.05	0.03 × 0.03 × 0.03	0.04 × 0.05 × 0.05
Theta range [°]	$3.214 \le \vartheta \le 30.574$	$1.932 \le \vartheta \le 26.476$	$2.895 \le \vartheta \le 29.997$	$2.876 \le \vartheta \le 28.993$	$2.917 \le \vartheta \le 29.633$
Index ranges *h*, *k*, *l*	$-9 \le h \le 8$ $-28 \le k \le 30$ $-9 \le l \le 6$	$-7 \le h \le 7$ $-52 \le k \le 52$ $-7 \le l \le 7$	$-9 \le h \le 5$ $-59 \le k \le 59$ $-8 \le l \le 8$	$-8 \le h \le 8$ $-57 \le k \le 57$ $-8 \le l \le 8$	$-8 \le h \le 8$ $-58 \le k \le 53$ $-8 \le l \le 8$
Reflections collected	5526	8730	9153	17335	5585
Independent reflections	780	1056	1441	1338	1390
Absorption correction	Multi-scan	Multi-scan	Multi-scan	Multi-scan	Multi-scan
Refinement method	Full-matrix least-squares on F^2	Full-matrix least-squares on F^2	Full-matrix least-squares on F^2	Full-matrix least-squares on F^2	Full-matrix least-squares on F^2
Refined parameters	35	77	85	81	87
Goodness of fit on F^2	1.131	1.137	1.115	1.126	1.204
$R1/\ wR^2$ (2σ)	0.0148/ 0.0298	0.0397/ 0.0957	0.0316/ 0.0734	0.0671/ 0.1473	0.0483/ 0.1052
$R1/\ wR^2$ (all data)	0.0176/ 0.0304	0.0520/ 0.1011	0.0334/ 0.0744	0.0711/ 0.1492	0.0509/ 0.1065
R_{int}	0.024	0.036	0.027	0.074	0.029
Largest diff. peak and hole [$e^-/Å^3$]	+1.156, –1.031	+4.802, –2.396	+3.246, –3.161	+4.869, –4.259	+4.007, –3.259

Table 4
Standardized atomic coordinates, isotropic (U_{eq}) and anisotropic (U_{ii}, U_{ij}, U_{jj}) displacement parameters for $LaZn_{1.50(1)}Sn_{1.98(2)}$ (defective $CaBe_2Ge_2$-type, *tP*10−x, x = 1.04; *P4/nmm*, No. 129) as obtained from single crystal analysis; $U_{23} = U_{12} = U_{13} = 0$.

Atom	Wyckoff site	Atomic coordinates			Occ.	U_{eq} [$Å^2$]	U_{11} [$Å^2$]	U_{22} [$Å^2$]	U_{33} [$Å^2$]
		x	*y*	*z*					
La	2*c*	1/4	1/4	0.75011(9)	1	0.0092(4)	0.0081(4)	0.0081(4)	0.0113(5)
Zn1	2*c*	1/4	1/4	0.3703(4)	0.496(10)	0.0189(15)	0.0225(19)	0.0225(19)	0.012(2)
Zn2	2*a*	3/4	1/4	0	1	0.0332(6)	0.0374(10)	0.0374(10)	0.0248(12)
Sn1	2*b*	3/4	1/4	1/2	1	0.0242(5)	0.0239(5)	0.0239(5)	0.0247(8)
Sn2	2*c*	1/4	1/4	0.1259(4)	0.494(7)	0.0097(8)	0.0085(5)	0.0085(5)	0.012(2)
Sn3	2*c*	1/4	1/4	0.1794(8)	0.449(5)	0.0097(8)	0.0085(5)	0.0085(5)	0.012(2)
Sn4	2*c*	1/4	1/4	0.235(6)	0.041(7)	0.0097(8)	0.0085(5)	0.0085(5)	0.012(2)

by contacting Cambridge Crystallographic Data Centre, 12 Union Road, Cambridge CB2 1EZ, UK; fax: +44 1223 336033.

2.4. Powder neutron diffraction (PND)

Powder neutron diffraction (PND) experiments were performed at the Fine Resolution Powder Diffractometer E9 (FIREPOD) at the research reactor of Helmholtz-Zentrum Berlin für Materialien und Energie, Berlin, Germany. The samples with nominal composition $La(Zn_{1-x}T_x)_2Sn_2$, with T = Ni and Cu and x = 0.5 were poured in vanadium containers and measured with a neutron wavelength of 1.7982 Å under ambient conditions. The Rietveld method was employed to refine the

Table 5
Standardized atomic coordinates, isotropic (U_{eq}) and anisotropic (U_{ii}, U_{ij}, U_{jj}) displacement parameters for $PrZn_{1.366(8)}Sn_{1.995(8)}$ (defective $CaBe_2Ge_2$-type, *tP*10−x, x = 1.278; *P4/nmm*, No. 129) as obtained from single crystal analysis; $U_{23} = U_{12} = U_{13} = 0$.

Atom	Wyckoff site	Atomic coordinates			Occ.	U_{eq} [$Å^2$]	U_{11} [$Å^2$]	U_{22} [$Å^2$]	U_{33} [$Å^2$]
		x	*y*	*z*					
Pr	2*c*	1/4	1/4	0.75021(6)	1	0.0076(2)	0.0072(2)	0.0072(2)	0.0083(3)
Zn1	2*c*	1/4	1/4	0.3713(5)	0.366(8)	0.0183(14)	0.0187(16)	0.0187(16)	0.018(2)
Zn2	2*a*	3/4	1/4	0	1	0.0325(5)	0.0366(8)	0.0366(8)	0.0243(10)
Sn1	2*b*	3/4	1/4	1/2	1	0.0241(3)	0.0214(4)	0.0214(4)	0.0294(7)
Sn2	2*c*	1/4	1/4	0.1227(4)	0.361(4)	0.0117(5)	0.0081(3)	0.0081(3)	0.0188(14)
Sn3	2*c*	1/4	1/4	0.1830(5)	0.591(7)	0.0117(5)	0.0081(3)	0.0081(3)	0.0188(14)
Sn4	2*c*	1/4	1/4	0.238(5)	0.043(6)	0.0117(5)	0.0081(3)	0.0081(3)	0.0188(14)

Table 6
Standardized atomic coordinates, isotropic (U_{eq}) and anisotropic (U_{11}, U_{22}, U_{33}, U_{12}, U_{23}, U_{13}) displacement parameters for $NdZn_{1.321(8)}Sn_{2.01(2)}$ (defective $CaBe_2Ge_2$-type, *tP*10−x, x = 1.59, *P4/nmm*, No. 129) as obtained from single crystal analysis; $U_{23} = U_{12} = U_{13} = 0$.

Atom	Wyckoff site	Atomic coordinates			Occ.	U_{eq} [Å^2]	U_{11} [Å^2]	U_{22} [Å^2]	U_{33} [Å^2]
		x	*y*	*z*					
Nd	2*c*	1/4	1/4	0.75014(16)	1	0.0076(5)	0.0071(5)	0.0071(5)	0.0085(7)
Zn1	2*c*	1/4	1/4	0.3724(1)	0.321(8)	0.012(2)	0.014(3)	0.014(3)	0.007(5)
Zn2	2*a*	3/4	1/4	0	1	0.0330(11)	0.0400(17)	0.0400(17)	0.018(2)
Sn1	2*b*	3/4	1/4	1/2	1	0.0240(7)	0.0217(8)	0.0217(8)	0.0285(15)
Sn2	2*c*	1/4	1/4	0.1200(10)	0.321(8)	0.0127(14)	0.0089(8)	0.0089(8)	0.020(4)
Sn3	2*c*	1/4	1/4	0.1832(9)	0.651(18)	0.0127(14)	0.0089(8)	0.0089(8)	0.020(4)
Sn4	2*c*	1/4	1/4	0.241(12)	0.042(15)	0.0127(14)	0.0089(8)	0.0089(8)	0.020(4)

Table 7
Lattice parameters (*a*, *c*), observed unit cell volume (V_{obs}) and volume contraction (ΔV %) for $RZn_{2-x}Sn_2$ (R = La, Ce, Pr, Nd) and $La(Zn,T)_{2-x}Sn_2$ (*T* = Mn, Fe, Co, Ni, Cu, Pd, Pt, Ag, Cd, Au).

$RZn_{2-x}Sn_2$	Space group	Pearson's symbol	a [Å]	b [Å]	c [Å]	V_{obs} [Å^3]	ΔV [%]
$LaZn_{1.50(1)}Sn_{1.98(2)}$	*P4/nmm*	*tP*10−x, x = 1.040	4.4895(1)	-	10.5823(5)	213.29(2)	6.27
$CeZn_{1.42(1)}Sn_{2.00}$*	*P4/nmm*	*tP*10−x	4.4588(2)	-	10.3564(9)	205.89(4)	6.82
$PrZn_{1.366(8)}Sn_{1.995(8)}$	*P4/nmm*	*tP*10−x, x = 1.278	4.4359(3)	-	10.301(1)	202.70(5)	7.28
$NdZn_{1.321(8)}Sn_{2.01(2)}$	*P4/nmm*	*tP*10−x, x = 1.590	4.420(0)	-	10.247(1)	200.19(2)	7.87
$LaZn_{1.18(1)}Mn_{0.38(1)}Sn_{2.02(2)}$	*P4/nmm*	*tP*10−x, x = 0.840	4.4924(4)	-	10.536(2)	212.63(5)	7.27
$LaZn_{1.18(1)}Fe_{0.38(1)}Sn_{2.00(2)}$	*P4/nmm*	*tP*10−x, x = 0.876	4.4872(2)	-	10.5360(6)	212.14(2)	7.18
$LaZn_{1.19(2)}Co_{0.33(3)}Sn_{1.993(4)}$	*P4/nmm*	*tP*10−x, x = 0.974	4.5043(4)	-	10.420(2)	211.41(5)	6.94
$LaZn_{1.18(1)}Ni_{0.38(1)}Sn_{1.98(2)}$	*P4/nmm*	*tP*10−x, x = 0.912	4.485(2)	-	10.465(6)	210.5(2)	6.93
$LaZnNi_{0.52(2)}Sn_2$**	*P4/nmm*	*tP*10−x	4.5016(1)	-	10.4689(1)	212.15(1)	5.63
$LaZn_{1.18(1)}Cu_{0.38(1)}Sn_{2.00(2)}$	*P4/nmm*	*tP*10−x, x = 0.880	4.4934(3)	-	10.572(1)	213.46(5)	6.35
$LaZnCu_{0.51(2)}Sn_2$**	*P4/nmm*	*tP*10−x	4.4972(1)	-	10.5612(4)	213.60(1)	5.37
$LaZnCu_{0.764(3)}Sn_{2.000(2)}$	*P4/nmm*	*tP*10−x, x = 0.418	4.4856(3)	-	10.6178(6)	213.64(3)	7.71
$LaZn_{1.11(1)}Pd_{0.44(2)}Sn_{2.01(2)}$	*P4/nmm*	*tP*10−x, x = 0.888	4.509(2)	-	10.556(8)	214.6(2)	6.84
$LaZn_{1.05(1)}Pt_{0.50(2)}Sn_{2.03(2)}$	*P4/nmm*	*tP*10−x, x = 0.832	4.5169(2)	-	10.4941(7)	214.10(2)	7.62
$LaZn_{1.446(1)}Sn_{2.000(1)}$ (LT)	*Cmmm*	*oC*40−x, x = 4.436	6.3181(8)	21.445(3)	6.3378(9)	858.7(2)	5.43
$LaZn_{1.15(1)}Ti_{0.42(1)}Sn_{2.00(1)}$	*Cmmm*	*oC*108−x, x = 34.936	6.357(6)	42.16(4)	6.337(6)	1699(3)	8.82
$LaZn_{1.099(4)}Ag_{0.36(1)}Sn_{2.00(1)}$	*Cmmm*	*oC*108−x, x = 36.644	6.4114(3)	42.215(2)	6.4023(3)	1732.8(1)	5.30
$LaZn_{1.323(7)}Cd_{0.17(2)}Sn_{2.01(2)}$	*Cmmm*	*oC*108−x, x = 35.884	6.369(1)	42.492(9)	6.363(1)	1722.0(5)	6.94
$LaZn_{1.360(3)}Au_{0.269(7)}Sn_{2.01(2)}$	*Cmmm*	*oC*112−x, x = 37.748	6.4108(3)	41.893(3)	6.3970(3)	1718.0(2)	8.25

(*) Composition from EDX data; (**) PND data.

PND data using the FULLPROF software package [30].

2.5. Differential thermal analysis (DTA)

Differential thermal analysis (DTA) was performed on a portion of 0.7–0.9 g of representative samples, either with nominal composition RZn_2Sn_2 or $R_2Zn_3Sn_4$. The specimens were enclosed in outgassed Mo crucibles (sealed by welding under an Ar flow) and then transferred to the DTA equipment (Netzsch 404 thermal analyzer). Thermal cycles were generally carried out with rates of 20 °C/min on heating and 10 °C/min (or 5 °C/min) on cooling; the accuracy in the temperature measurements was ± 5°C.

2.6. Physical property measurements

The magnetization data both as a function of temperature, M(T) and applied magnetic field, M(H), were collected using a Magnetic Properties Measurement System (MPMS, SQUID magnetometer) and a vibrating sample magnetometer (VSM) (both from Quantum Design, Inc., USA). The specific heat, C_P, was measured by relaxation method using the heat capacity option of a commercial Physical Property Measurement System (PPMS, Quantum Design). The electrical resistivity, ρ, was measured at zero and applied magnetic field using standard four-probe technique using the AC transport option of a PPMS; the measurements were carried out by setting the direction of the electric current orthogonal to the applied magnetic field.

2.7. DFT calculations

Tight-binding electronic structure calculations were performed according to the linear muffin-tin-orbital (LMTO) method in the atomic sphere approximation (ASA). An idealized model for $LaZn_{1.5}Sn_2$ - $LaZn_2Sn_2$ with full occupation of all Zn positions and no positional disorder of the Sn position has been applied (only the Sn2 position was kept). Basis sets of La 6*s*, (6*p*), 5*d*, 4*f*, Zn 4*s*, 4*p*, 3*d*, and Sn 5*s*, 5*p*, (5*d*) (downfolded orbitals in parentheses) were employed. Scalar relativistic effects were included in the calculations. The band structures were sampled for 4608 k points in the irreducible wedge of the Brillouin zone. The radii of the Wigner-Seitz spheres were assigned automatically so that the overlapping potentials would be the best possible approximations to the full potentials. They were determined to be 2.28 Å for La, 1.35 Å for Zn and 1.58 and 1.63 Å for Sn.

3. Results and discussion

3.1. Phase formation of $RZn_{2-x}Sn_2$ and $La(Zn,T)_{2-x}Sn_2$

The rare-earth intermetallic compound with $RZn_{2-x}Sn_2$ stoichiometry has been identified in the ternary R-Zn-Sn system for the light lanthanides (R = La, Ce, Pr, and Nd), but Sm. In the Ce samples prepared with nominal composition $CeZn_2Sn_2$ and $Ce_2Zn_3Sn_4$, we confirmed the formation of the $CeZn_{2-x}Sn_2$ compound, while the existence of the stoichiometric 1:2:2 phase reported in the Ce-Zn-Sn system [23] was disproved. Sm does not form this phase likely due to geometric reasons. In contrast, Eu forms a stoichiometric $EuZn_2Sn_2$ [24] that is consistent with its divalent character. Thermal analysis (DTA) suggests these

Table 8
Interatomic distances for $d_{obs}/\Sigma r_M \leq 1.00$) in $LaZn_{1.50(1)}Sn_{1.98(2)}$, $PrZn_{1.366(8)}Sn_{1.995(8)}$, $NdZn_{1.321(8)}Sn_{2.01(2)}$ and in the substituted $LaZn_{1.18(1)}Cu_{0.38(1)}Sn_{2.00(2)}$.

$LaZn_{1.50(1)}Sn_{1.98(2)}$				$LaZn_{1.18(1)}Cu_{0.38(1)}Sn_{2.00(2)}$				$PrZn_{1.366(8)}Sn_{1.995(8)}$				$NdZn_{1.321(8)}Sn_{2.01(2)}$			
Central atom	**Ligands**	**d [Å]**	**$d_{obs}/\Sigma r_M$**	**Central atom**	**Ligands**	**d [Å]**	**$d_{obs}/\Sigma r_M$**	**Central atom**	**Ligands**	**d [Å]**	**$d_{obs}/\Sigma r_M$**	**Central atom**	**Ligands**	**d [Å]**	**$d_{obs}/\Sigma r_M$**
La (2*c*)	4 Sn1	3.4705	0.992	La (2*c*)	4 Sn1	3.4745	0.993	Pr (2*c*)	4 Sn1	3.4003	0.985	Nd (2*c*)	4 Sn1	3.3841	0.983
	4 Sn2	3.4350	0.981		4 Sn2	3.4340	0.981		4 Sn2	3.3989	0.985		4 Sn2	3.3979	0.987
	4 Sn3	3.2610	0.932		4 Sn3	3.2892	0.940		4 Sn3	3.2112	0.930		4 Sn3	3.1967	0.928
	4 Sn4	3.1785	0.908		4 Sn4	3.2198	0.920		4 Sn4	3.1390	0.910		-	-	-
Zn1 (2*c*)	4 Sn1	2.6311	0.872	Zn1 (2*c*)	4 Sn1	2.6227	0.869	Zn1 (2*c*)	4 Sn1	2.5840	0.856	Zn1 (2*c*)	4 Sn1	2.5673	0.851
	1 Sn2	2.5863	0.857		1 Sn2	2.6001	0.862		1 Sn2	2.5608	0.849		1 Sn2	2.5894	0.858
	1 Sn3	2.0202	0.670		1 Sn3	2.1478	0.712		1 Sn3	1.9397	0.643		1 Sn3	1.9275	0.939
	1 Sn4	1.4318	0.475		1 Sn4	1.8185	0.603		1 Sn4	1.3731	0.455		-	-	-
Zn2 (2*a*)	4 Sn3	2.9399	0.974	Zn2/Cu (2*a*)	4 Sn3	2.8695	0.964	Zn2 (2*a*)	4 Sn3	2.9108	0.965	Zn2 (2*a*)	4 Sn2	2.5281	0.938
	4 Sn2	2.6104	0.865		4 Sn2	2.6123	0.878		4 Sn2	2.5528	0.846		4 Sn3	2.9077	0.964
Sn1 (2*b*)	4 La	3.4705	0.992	Sn1 (2*b*)	4 La	3.4745	0.993	Sn1 (2*b*)	4 Pr	3.4003	0.985	Sn1 (2*b*)	4 Nd	3.3841	0.983
	4 Zn1	2.6311	0.872		4 Zn1	2.6227	0.869		4 Zn1	2.5840	0.856		4 Zn1	2.5673	0.851
	4 Sn1	3.1746	0.978		4 Sn1	3.1773	0.979		4 Sn1	3.1367	0.966		4 Sn1	3.1254	0.963
Sn2 (2*c*)	4 La	3.4350	0.981	Sn2 (2*c*)	4 La	3.4340	0.981	Sn2 (2*c*)	4 Pr	3.3989	0.985	Sn2 (2*c*)	4 Nd	3.3979	0.987
	1 Zn1	2.5863	0.857		1 Zn1	2.6001	0.862		1 Zn1	2.5608	0.849		1 Zn1	2.5894	0.858
	4 Zn2	2.6104	0.865		4 Zn2/Cu	2.6123	0.878		4 Zn2	2.5528	0.846		4 Zn2	2.5281	0.938
	1 Sn3	0.5662	0.174		1 Sn3	0.4523	0.139		1 Sn3	0.6212	0.191		1 Sn3	0.6620	0.204
	1 Sn4	1.1545	0.356		1 Sn4	0.7816	0.241		1 Sn4	1.1877	0.366		-	-	-
Sn3 (2*c*)	4 La	3.2610	0.932	Sn3 (2*c*)	4 La	3.2892	0.940	Sn3 (2*c*)	4 Pr	3.2112	0.930	Sn3 (2*c*)	4 Nd	3.1967	0.928
	1 Zn1	2.0202	0.670		1 Zn1	2.1478	0.712		1 Zn1	1.9397	0.643		1 Zn1	1.9275	0.939
	4 Zn2	2.9399	0.974		4 Zn2/Cu	2.8695	0.964		4 Zn2	2.9108	0.965		4 Zn2	2.9077	0.964
	1 Sn2	0.5662	0.174		1 Sn2	0.4523	0.139		1 Sn2	0.6212	0.191		1 Sn2	0.6620	0.204
	1 Sn4	0.5884	0.181		1 Sn4	0.3293	0.101		1 Sn4	0.5666	0.175		-	-	-
Sn4 (2*c*)	4 La	3.1785	0.908	Sn4 (2*c*)	4 La	3.2198	0.920	Sn4 (2*c*)	4 Pr	3.1390	0.910	-	-	-	-
	1 Zn1	1.4318	0.475		1 Zn1	1.8185	0.603		1 Zn1	1.3731	0.455		-	-	-
	1 Sn2	1.1545	0.356		1 Sn2	0.7816	0.241		1 Sn2	1.1877	0.366		-	-	-
	1 Sn3	0.5884	0.181		1 Sn3	0.3293	0.101		1 Sn3	0.5666	0.175		-	-	-

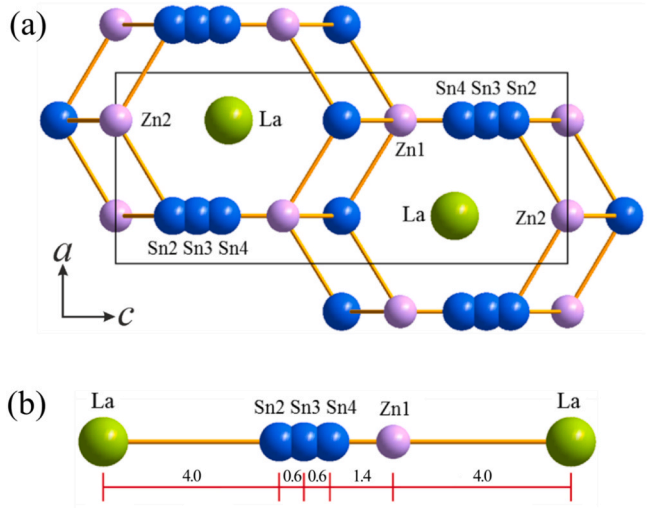

Fig. 3. (a) Projection of the crystal structure of $LaZn_{2-x}Sn_2$ on the *ac*-plane. (b) Interatomic distances in the crystal structure of $LaZn_{2-x}Sn_2$ along the *c*-axis involving all disordered Sn and Zn positions.

phases form by a peritectic reaction. The type of formation, together with the high volatility of Zn, may explain the origin of experimental difficulties in obtaining a single-phase product for these materials. A typical representative DTA cycle, recorded on a nearly single-phase sample with nominal composition $La_{22.2}Zn_{33.3}Sn_{44.4}$ (annealed at 850°C, slowly cooled), is shown in Fig. 1.

As expected, upon heating, a more pronounced peak starts at 915°C, corresponding to the decomposition of the $LaZn_{2-x}Sn_2$ formed after annealing; this is then followed by a second thermal effect at 945°C and a final shoulder at about 1000°C (for this last effect the temperature is not reported in the Figure). Differently, three stronger thermal effects occur on cooling: a first and weaker peak at 995°C, followed by at least two subsequent stronger peaks at 945°C and 910°C. These thermal effects, associated with analysis of also the microstructure of the sample and the EDX microanalytical data of the resulting phases, can likely be ascribed to the formation of the different compounds in the following way. The peak at 995°C is relative to the formation of the new pseudoternary $La(Zn_xSn_{1-x})_3$ [cubic $AuCu_3$-type, *cP*4, *Pm*−3 *m*, No. 221] phase, the peak at 945°C is due to the formation of $LaZn_{13}$ [cubic $NaZn_{13}$-type, *cF*112, *Fm*−3*c*, No. 226] [34], and the peak at 910°C should be pertinent to the formation of the new $LaZn_{1.5}Sn_2$ ternary compound (with undercooling effects of about 10°C). Besides, at least two further weak and broader peaks emerge both on heating and cooling (545 and 565°C on heating, and 550 and 520°C on cooling). These can be thought as associated to eutectic reactions and/or to structural transitions; however a much deeper study is required to shed full light on their origin.

SEM-EDX analysis carried out on this sample after DTA corroborated the typical peritectic microstructural morphology of these new intermetallic compounds. The SEM images showing the microstructure of selected areas of the samples $La_{22.2}Zn_{33.3}Sn_{44.5}$, $Ce_{22.2}Zn_{33.3}Sn_{44.5}$, and the substituted samples with nominal composition $LaZn_{1.2}Cu_{0.4}Sn_2$ ($La_{21.7}Zn_{26.1}Cu_{8.7}Sn_{43.5}$) and $LaZn_{1.2}Cd_{0.4}Sn_2$ ($La_{21.7}Zn_{26.1}Cd_{8.7}Sn_{43.5}$) are shown in Figs. 2**a-d**. In all samples, three phases are visible, with the main one (as the matrix) being the new tetragonal phase with average elemental composition $La_{22.0}Zn_{33.2}Sn_{44.8}$ (Fig. 2**a**), $Ce_{22.2}Zn_{33.3}Sn_{44.5}$ (Fig. 2**b**), $La_{22.0}Zn_{26.2}Cu_{8.6}Sn_{43.2}$ ($LaZn_{1.19}Cu_{0.39}Sn_{1.96}$) (Fig. 2**c**) and $La_{22.0}Zn_{31.0}Cd_{3.4}Sn_{43.6}$ ($LaZn_{1.41}Cd_{0.15}Sn_{1.98}$) (Fig. 2**d**). The dark grains correspond to the binary $LaZn_{13}$, $CeZn_{13}$, $LaZn_{13-x}Cu_x$ and $LaZn_{13-x-y}Cu_xCd_y$ phases, respectively for the four samples, and the light-gray grains present in small amount pertain to the binary $LaSn_3$, $CeSn_3$ and pseudobinary $La(Zn_xSn_{1-x})_3$ and $La(Zn_xCd_ySn_{1-x-y})_3$ phases [containing up to 7 and 3 at% Zn for $La(Zn_xSn_{1-x})_3$ and $La(Zn_xCd_ySn_{1-x-y})_3$, respectively] for the four samples, respectively. The EDX microprobe analysis indicated a stoichiometry of, or very close to $LaZn_{1.5}Sn_2$, $CeZn_{1.5}Sn_2$, $LaZn_{1.2}Cu_{0.4}Sn_2$ and $LaZn_{1.4}Cd_{0.2}Sn_2$ for the four new ternary and pseudoternary compounds, with a negligible solid solubility range of Zn in $LaZn_{1.5}Sn_2$, and $CeZn_{1.5}Sn_2$.

3.2. *Crystal structure of $RZn_{2-x}Sn_2$ and $La(Zn,T)_{2-x}Sn_2$*

3.2.1. *Tetragonal $RZn_{2-x}Sn_2$*

The single crystals for the structural study and refinements have been

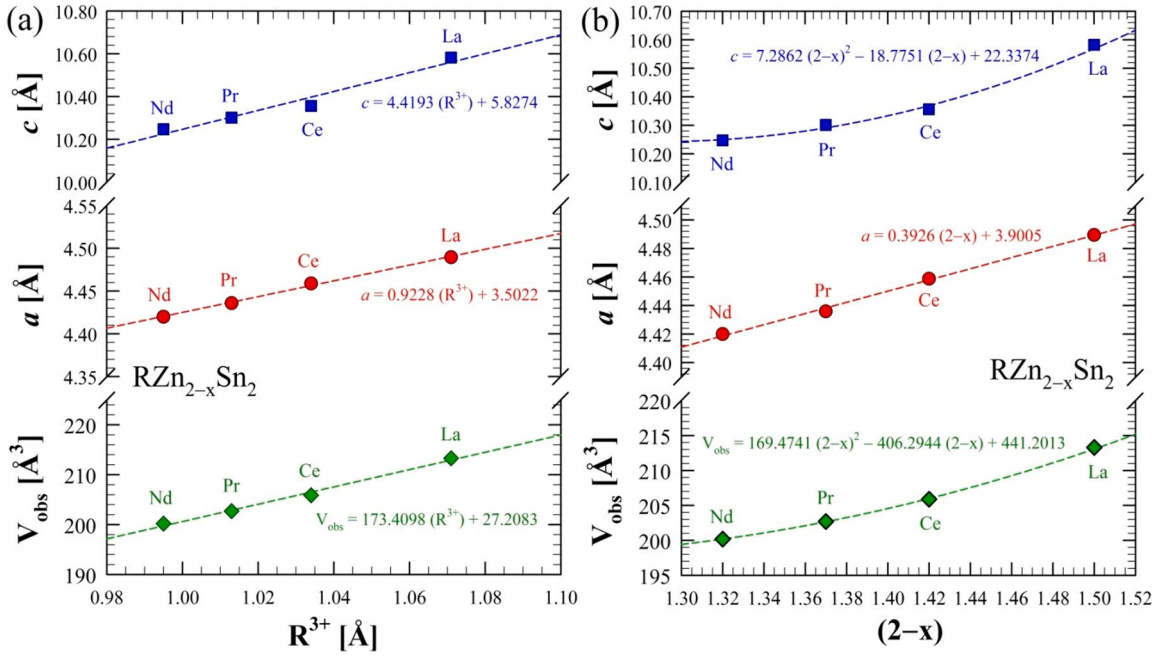

Fig. 4. The trend of the lattice parameters (*a* and *c*) and unit cell volume (V_{obs}) *vs.* the R^{3+} ionic radius (a) and the Zn content per formula (b) for the $RZn_{2-x}Sn_2$ compounds (R = La-Nd).

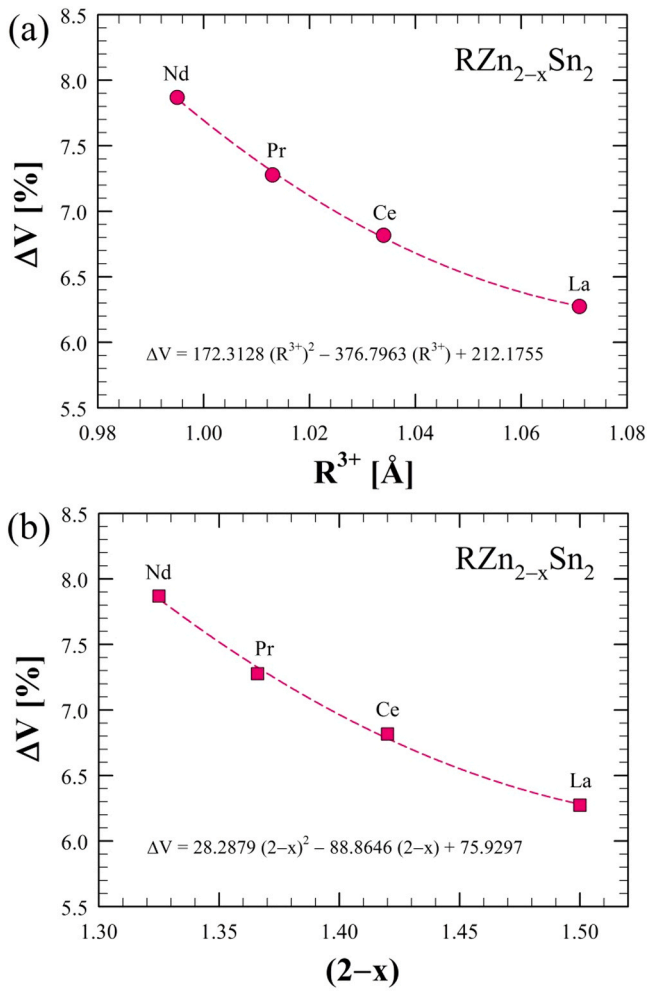

Fig. 5. Trend of the volume of formation (ΔV %) *vs.* the R^{3+} ionic radius (a) and the (2−x) coefficient (b) for the $RZn_{2-x}Sn_2$ compounds (R = La, Ce, Pr, Nd).

isolated from the ternary $RZn_{2-x}Sn_2$ samples with R = La, Pr, and Nd, and for the substituted $La(Zn_{1.2}T_{0.4})Sn_2$ samples with T = Ti, Mn, Fe, Co, Ni, Cu, Pd, Pt, Ag, Au and Cd. The single crystal data, along with the refinement details and resulting stoichiometries, are all collected in Table 1 for the ternary $RZn_{2-x}Sn_2$ compounds and in Tables 2–3 for the $La(Zn_{1.2}T_{0.4})Sn_2$ pseudoternary phases. The structure for the compounds with T = Ni and Cu has also been refined by using the Rietveld method on X-ray and neutron diffraction powder data. X-ray diffraction studies revealed the crystal structure of the $RZn_{2-x}Sn_2$ compounds to be a defect derivative of the $CaBe_2Ge_2$-type, which is closely related to the $UCo_{1.5}Sn_2$ structure type [25], with substantial defects and disorder. However, the model that best illustrates the structure of $LaZn_{1.5}Sn_2$ is the $CaBe_2Ge_2$-type and not the $UCo_{1.5}Sn_2$. The R atoms occupy the 2*c* Wyckoff site (occupied by Ca atoms in $CaBe_2Ge_2$), Zn atoms occupy the two 2*a* and 2*c* positions (occupied by Ge atoms in the prototype) and Sn atoms occupy the two 2*b* and 2*c* sites (occupied by Be atoms in the prototype). The 2*a* (Zn2) and 2*b* (Sn1) positions are tetrahedrally coordinated (Zn@Sn_4 and Sn@Zn_4), while the 2*c* position (Zn1 and Sn2) is pyramidally coordinated (Zn@Sn_5 and Sn@Zn_5). In contrast to the prototype, the Sn2 (2*c*) position splits over three locations (Sn2, Sn3 and Sn4) for the La, Pr and Nd compounds. The refined stoichiometries of the ternary $RZn_{2-x}Sn_2$ compounds show an interesting correlation between the R size and Zn content along the series. While Sn overall retains full occupation and in all the four compounds its stoichiometric coefficient remains practically the same and fixed at 2, the Zn content decreases along the series from ≈ 1.50 in $LaZn_{1.50(1)}Sn_{1.98(2)}$ to ≈ 1.32 in $NdZn_{1.321(8)}Sn_{2.01(2)}$ due to the occupation of the Zn1 (2*c*) site [which drops from ≈ 50% in the La compound (Table 4) to ≈ 42%, ≈ 37% and ≈ 32% in the Ce, Pr and Nd compounds, respectively (Tables 5 and 6) (EDX data for Ce compound)]. The evident decrease of the occupation factor of the Zn1 (2*c*) site in the $RZn_{2-x}Sn_2$ series directly reflects the effect of the lanthanide contraction which brings the compounds to their more stable thermodynamic configuration by lowering the Zn content giving another hint regarding the missing Sm representative. The lattice parameters of these ternary compounds and interatomic distances are reported in Tables 7 and 8, respectively.

A projection of the crystal structure for $LaZn_{1.5}Sn_2$, along the *b*-axis, is shown in Fig. 3**a**, while the interatomic distances along the *c*-axis, involving the disordered Sn and Zn sites, are represented in Fig. 3**b**.

The trend of the lattice parameters (*a* and *c*) and the observed unit cell volume (V_{obs}) as a function of the R^{3+} ionic radius [35] is shown in Fig. 4**a**. Both lattice parameters and unit cell volume linearly decrease from La to Nd perfectly following the lanthanide contraction trend. A correlation is also found between either the lattice parameters or unit cell volume and the stoichiometric coefficient (2−x) of Zn and so x; in this regard, while the parameter *a* linearly increases while increasing (2−x) (decreasing x), both the parameter *c* and V_{obs} increase as a function of (2−x) by following a quadratic trend (Fig. 4**b**).

The volume of formation values {ΔV %, where $\Delta V = [(V_{obs} - V_{calc})/V_{calc} \times 100]$; V_{calc} is the volume of the compound calculated from the atomic volumes of the individual atoms [36]} for the $RZn_{2-x}Sn_2$ compounds (R = La, Ce, Pr, Nd) are collected in Table 7. As expected, the absolute value of the volume of formation, ΔV %, increases along the lanthanide series from La to Nd; such an increase follows a quadratic trend (Fig. 5**a**). Interestingly, the ΔV % as a function of the Zn content (expressed as 2−x) increases by following a quadratic trend along the series from the La to the Nd compound (Fig. 5**b**). As the ΔV % is proportional to the formation enthalpy of a compound [37,38], these two trends suggest that the thermodynamic stability of the $RZn_{2-x}Sn_2$ compounds would increase on going from the La to the Nd compound.

3.2.2. *Tetragonal $La(Zn,T)_{2-x}Sn_2$*

A significantly more complex picture has been observed in the structure of the quaternary (pseudoternary) compounds $La(Zn,T)_{2-x}Sn_2$ (with T = Mn, Fe, Co, Ni, Cu, Pd, Pt), whose atomic coordinates and site occupancies from single crystal data are collected in Tables S1-S7. Also, these quaternary phases adopt the derivative $CaBe_2Ge_2$-type structure (*t*P10, *P4/nmm*). In all these phases, the T element replaces Zn atoms in the Zn1 (2*c*) position giving rise to a broad compositional range (Zn/T) depending on the T element; the Zn/T ratio ranges from 1.31 in $LaZnCu_{0.764(3)}Sn_{2.000(2)}$ (Table S6) to 2.20 in $LaZn_{1.05(1)}Pt_{0.50(1)}Sn_{2.03(2)}$ (Table S8), 2.53 in $(LaZn_{1.11(1)}Pd_{0.44(3)}Sn_{2.01(12)}$ (Table S7), 3.15 in $LaZn_{1.18(1)}Mn_{0.38(1)}Sn_{2.02(2)}$, $LaZn_{1.18(1)}Fe_{0.38(1)}Sn_{2.00(2)}$, $LaZn_{1.18(1)}Ni_{0.38(1)}Sn_{1.98(2)}$ and $LaZn_{1.18(1)}Cu_{0.38(1)}Sn_{2.00(2)}$ (Table S1, S2, S4 and S5) up to 3.61 in $LaZn_{1.19(3)}Co_{0.33(3)}Sn_{1.99(1)}$ (Table S3). For the $La(Zn,T)_{2-x}Sn_2$ compounds formed by heavier T elements (T = Pd, Pt) the crystal structure can be better described by considering, in addition to the Zn1 (2*c*) and Sn2–4 (2*c*) sites, also the Zn2 (2*a*) as a disordered site, and two more Wyckoff positions with 8*i* symmetry, little occupied by T (Pd3 or Pt3) and Zn (Zn3) atoms, respectively. The central position 2*a* (Zn2) with a relatively high occupation, and the two low occupied 8*i* positions (*T*3 and Zn3, respectively), forming two tetrahedra, give a total occupation of all these three positions [Zn1 (2*c*), *T*3 (8*i*) and Zn2 (2*c*)] approaching one fully occupied 2*a* position, similarly to all other compounds in this series. Rietveld refinement was carried out on the X-ray powder patterns of two samples with nominal composition $LaZn_{1.5}Sn_2$ and $LaZn_{1.2}Cu_{0.4}Sn_2$. The Rietveld profiles are shown in Figs. 6**a** and **b**, respectively; the main and secondary or extra phases in each sample are given in the corresponding captions. In the $LaZn_{1.5}Sn_2$ sample the presence of significant amounts of an orthorhombic modification accompanying the tetragonal phase was ascertained. However, the relative amounts of the orthorhombic phase compared to the tetragonal

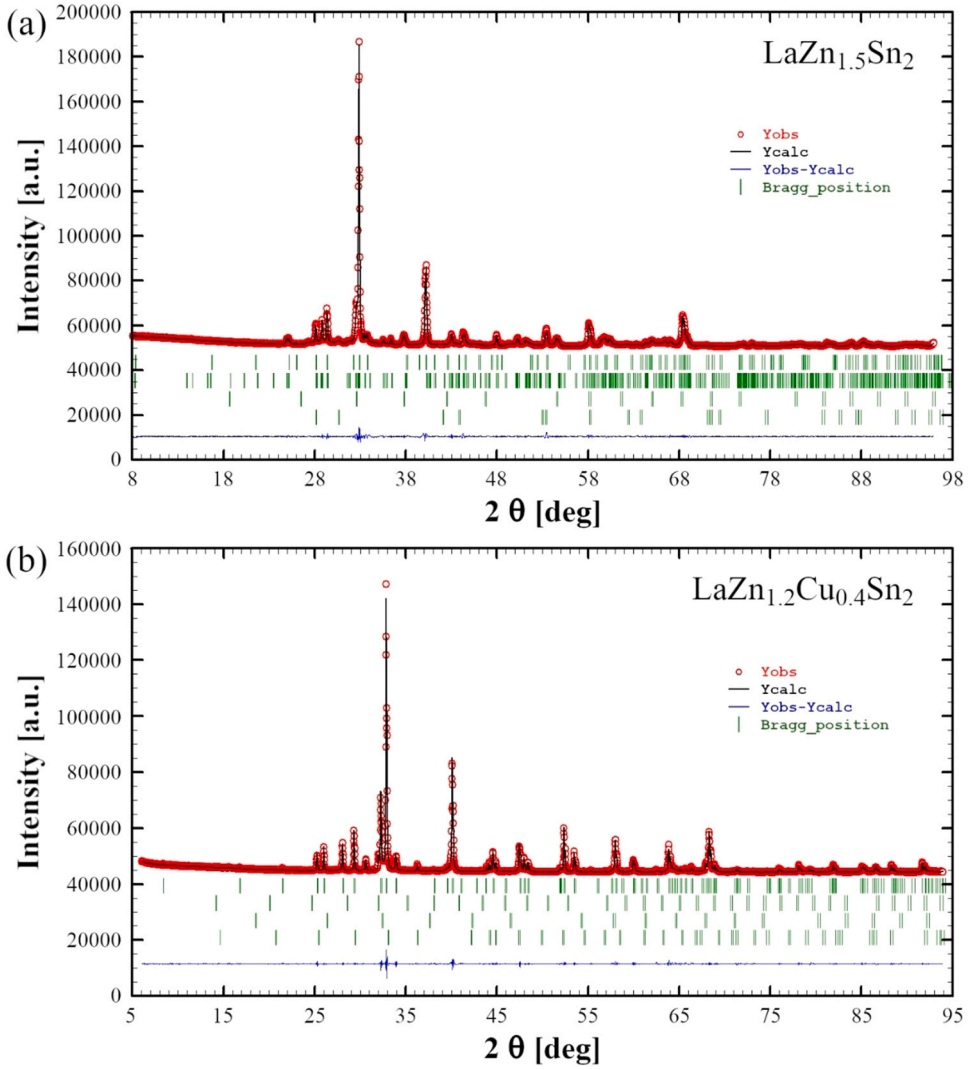

Fig. 6. Observed X-ray powder pattern (red circle) and Rietveld refinement profile (black line) for the samples with nominal composition $LaZn_{1.5}Sn_2$ (annealed at 900°C - 4 days) (**a**) and $LaZn_{1.2}Cu_{0.4}Sn_2$ (annealed at 850°C for 7 days) (**b**). The lower profile (blue line) gives the difference between observed and calculated data; the Bragg angle positions are indicated by vertical bars (green). In the patter for the sample $LaZn_{1.5}Sn_2$ (**a**), the upper Bragg positions row indicates the tetragonal $LaZn_{1.50}Sn_2$ phase, the second row indicates the orthorhombic $LaZn_{1.45}Sn_{2.00}$ phase, the third row is related to $LaZn_xSn_{3-x}$ (with x = 0.28, as from EDX data) and the lower row indicates Sn. In the pattern for the sample $LaZn_{1.2}Cu_{0.4}Sn_2$ (**b**), the upper Bragg positions indicate the tetragonal $LaZn_{1.2}Cu_{0.4}Sn_2$ phase, the second row indicates the limit of solid solubility of the cubic $Cu_{5-x}Zn_{8+y}$ phase with composition 'CuZn$_2$' (as from EDX data), the third row is related to the cubic $LaZn_xSn_{3-x}$ (with x = 0.11, as from EDX data), and the lower row indicates the cubic $LaZn_{13-x-y}Cu_xSn_y$ phase (with x = 11.11 and y = 1.68, as from EDX data).

one could not be determined accurately due to strong overlapping of many reflections (most of the strongest peaks, see Fig. 6**a**). The presence of the orthorhombic form alongside the tetragonal one in the $LaZn_{1.2}Cu_{0.4}Sn_2$ sample remains doubtful and questionable, as no peak could be distinctly assigned to the orthorhombic phase alone (Fig. 6**a**).

To further investigate which of the two 2*a* and 2*c* Zn sites *T* atom substitutes Zn in the quaternary compound, PND measurements were carried out on two $La(Zn_{1-x}T_x)_2Sn_2$ samples for T = Ni and Cu and x = 0.5. Due to their nearly identical X-ray atomic scattering factor, it is impossible to distinguish Ni and Cu from Zn using X-ray diffraction. Neutron diffraction, instead, allows us to clearly discriminate these elements thanks to the large difference in their scattering lengths. The Ni-doped sample was added to the experiment because the Ni-Zn scattering length difference is more than twice as large as that for Cu-Zn and, therefore, it makes it even easier to differentiate between these two elements. Restrictions were imposed on the refinements to guarantee physically reasonable results. Sn3 and Sn4 were combined into one shared crystallographic site since Sn4 is too little occupied to be reliably resolved using powder diffraction. As Sn2 and Sn3/4 are split positions, they were refined to have a full occupation in total. At last, the occupations of Zn1 and Sn2 were coupled to ensure plausible Zn-Sn distances. Refinements of the PND data clearly show that both Ni and Cu only occupy the partially filled Zn1 (2*c*) site. The scattering contribution to the Zn1 position is strong and indicates, in combination with the PXRD refinements carried out on the same samples used for neutron scattering, that Zn is completely replaced by Ni and Cu and no Zn is detected in the 2*c* site. The final compositions of the two quaternary compounds are $LaZnNi_{0.52(2)}Sn_2$ and $LaZnCu_{0.52(2)}Sn_2$ (Table 7). The Cu occupation in the 2*c* site can reach up to ≈ 80% [in $LaZnCu_{0.791(3)}Sn_2$], which is much higher than the maximal occupation of 50% observed in the case of the ternary $LaZn_{2-x}Sn_2$ [in $LaZn_{1.50(1)}Sn_{1.98(2)}$]; the high occupation degree of the 2*c* site by Cu in $LaZnCu_{0.791(3)}Sn_2$ may be due to the smaller atomic volume of Cu atoms compared to Zn [36]. The full stoichiometric $LaZnTSn_2$ could not be obtained under analogous synthetic conditions, likely due to geometric restrictions. The Rietveld refinement fit on the neutron powder pattern for these two compounds is shown in Figs. 7**a** and **b**, respectively. Similarly to the ternaries, in the pseudoternary $La(Zn,T)_{2-x}Sn_2$ the site occupation of Zn and disordered

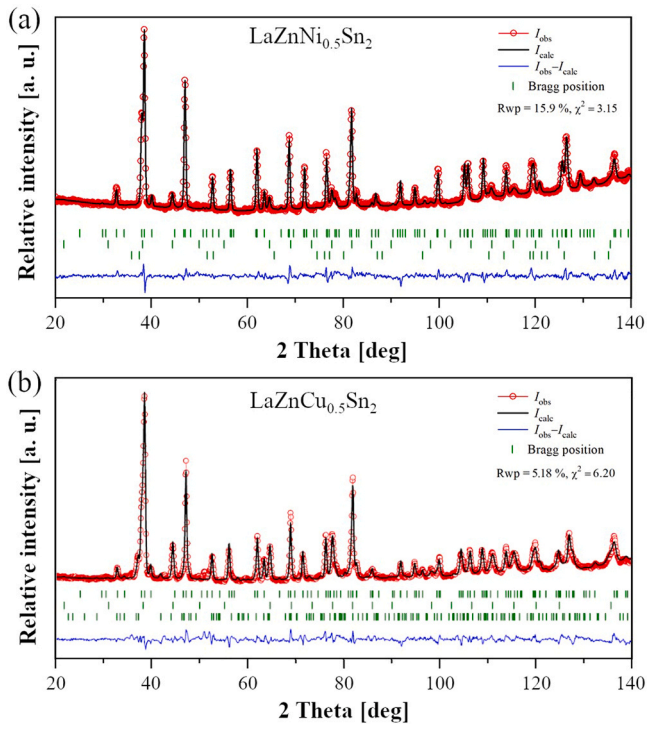

Fig. 7. Observed neutron powder patterns (red circle), and Rietveld refinement profile (black line) for the samples with nominal composition $LaZnNi_{0.5}Sn_2$ (top) and $LaZnCu_{0.5}Sn_2$ (bottom). The lower profile (blue line) gives the difference between observed and calculated data. The Bragg angle positions are indicated by vertical bars (green). For the Ni sample, the composition was $LaZnNi_{0.52(2)}Sn_2$ 87(2) wt% (upper row), $LaSn_3$ 12.0(8) wt% (middle row) and Sn 1.0(5) wt% (bottom row). For the Cu sample, the composition was $LaZnCu_{0.51(2)}Sn_2$ 70.1(2) wt% (upper row), $LaSn_3$ 20.9(3) wt% (second row), and $LaCu_{0.5}Sn_2$ 9.0(3) wt% (bottom row).

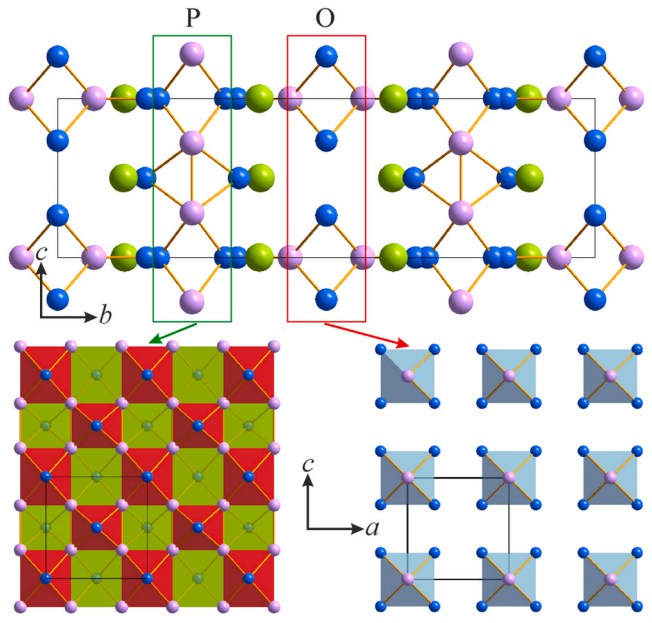

Fig. 8. Projection of the crystal structure of orthorhombic $LaZn_{1.445(2)}Sn_2$ on the *ac*-plane. The octahedral layer is outlined in a red box, while the pyramidal one is in green. La atoms are green, Zn are purple and Sn are blue.

Sn positions are highly correlated and directly linked to the combination of R or *T* elements involved; again, mostly resulting from size effects. Lattice parameters of also all the pseudoternary compounds, and interatomic distances, are reported in Tables 7 and 8, respectively.

The interatomic distances for $d_{obs}/\Sigma rM \leq 1.00$ (where d_{obs} is the observed interatomic distance between two next neighbor atoms and $/\Sigma rM$ is the sum of the two metallic radii) of some selected compounds [*i.e.*, $LaZn_{1.50(1)}Sn_{1.98(2)}$, $PrZn_{1.366(8)}Sn_{1.995(8)}$, $NdZn_{1.321(8)}Sn_{2.01(2)}$ and the substituted $LaZn_{1.175(3)}Cu_{0.360(3)}Sn_{2.002(5)}$] are collected in Table 8. The volume of formation values, ΔV %, for all the pseudoternary La(Zn, T)$_{2-x}$Sn$_2$ (*T* = Mn, Fe, Co, Ni, Cu, Pd, Ag, Pt, Au, Cd) phases are also in Table 8. The composition of each phase reported in the table was obtained from either single crystal refinement or EDX or PND data. The values range between about 5.4% and 7.7% depending on the *T* metal and Zn/*T* compositional ratio.

3.2.3. *Orthorhombic modification of $LaZn_{2-x}Sn_2$ and $La(Zn,T)_{2-x}Sn_2$*

Along with the crystals of the tetragonal $LaZn_{1.50(1)}Sn_{1.98(2)}$ phase, crystals of an orthorhombic compound have also been detected in the same sample. The refined composition for the orthorhombic phase, $LaZn_{1.445(2)}Sn_2$, is very close to that of the tetragonal phase, but it seems to show lower Zn content. The formation of the orthorhombic $LaZn_{1.445(2)}Sn_2$ may be thermodynamically favored by either a slightly lower Zn composition than that necessary to form the tetragonal phase or by a lower annealing temperature. The cooling rate after melting may also play a role in its formation, because of the peritectic formation of the tetragonal $LaZn_{1.5}Sn_2$: a slower cooling can likely allow the congruently-melting extra-phase $LaZn_xSn_{3-x}$ to crystallize with higher Zn contents (this leaving the remaining molten poorer in Zn). At present, although a definitive explanation on the parameters that drive the formation of the orthorhombic phase remains an unresolved question. In light of the DTA data (Paragraph 3.1.), we plausibly assume that the temperature factor is the most important and that it forms at temperatures even lower than those of the tetragonal as never present in the samples as the predominant one. This phase crystallizes in the space group *Cmmm* (No. 65) and exhibits a practically 4-fold unit cell of the former ($a^* \approx a\sqrt{2}$, $c^* \approx 2c$); the lattice parameters are reported in Table 3. The prototype is its own, with Pearson's symbol *oC*40−x (x = 4.436). The unit cell contains two Wyckoff positions for La atoms with 4*j* and 4*i* symmetry, two atomic sites for Zn atoms with 8 *m* and 4*i* symmetry (the 8 *m* site being fully occupied and the 4*i* site being partially vacant), and four atomic positions for Sn atoms with 8*o*, 4*j* and 4*i* symmetry (among them the 8*o* and 4*j* being fully occupied and the two 4*i* ones being partially vacant). The refined atomic coordinates and details about the crystal structure are listed in Table S9. PXRD patterns of both phases showed practically full overlap suggesting close structural relationships. Surprisingly though, both space groups do not exhibit any group-subgroup relationships. The crystal structure of the orthorhombic $LaZn_{1.445(2)}Sn_2$ represents a new structure type and is best represented as an intergrowth of two different types of anionic layers, with only one of them keeping structural vicinity with the prototype (Fig. 8). One of the layers (green box) exhibits identical motifs - checkered (up and down, Fig. 8: red and green) Zn_4Sn distorted square pyramids, although half of them are somewhat squashed due to the atomic arrangement in the second layer. This layer is easier understood as a plane with a rectangular arrangement of the Zn atoms capped by Sn atoms. The squares observed in the crystal structure of the tetragonal $LaZn_{1.50(1)}Sn_{1.98(2)}$ phase are slightly distorted, thus causing the loss of the tetragonal symmetry. In contrast, the other layer is represented by an identical Sn plane. In this case, Zn atoms cap the Sn rectangles but simultaneously above and below forming Zn_2Sn_4 octahedra. Each octahedron is surrounded by eight empty rectangles, meaning only 25% of squares are capped. Therefore if the former layer can be summarized as ZnSn, the latter one can be summarized as $ZnSn_2$. The Zn_2Sn_4 octahedra directly affect the shape of the Zn_4Sn pyramids from the first layer resulting in their squeezing and alternation of the Zn-

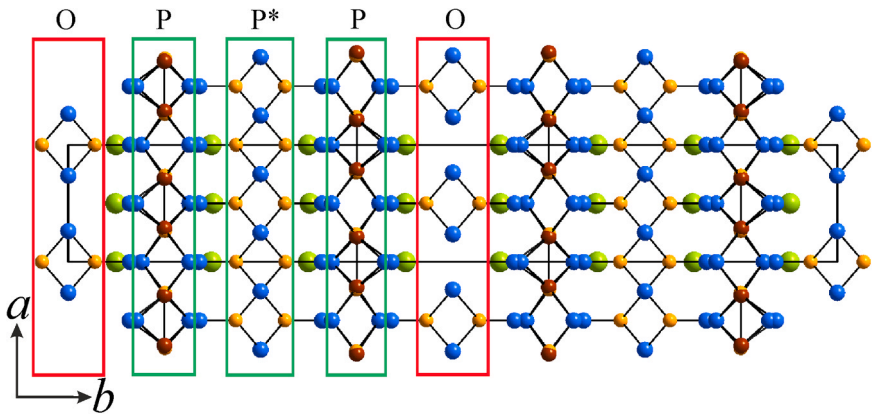

Fig. 9. Projection of the crystal structure of $LaZn_{1.10(1)}Ag_{0.36(1)}Sn_2$ on the *ab* plane. La atoms are green, Zn – orange, Ag – brown, and Sn – blue. The octahedral layers are outlined in red boxes, while the pyramidal ones are in green.

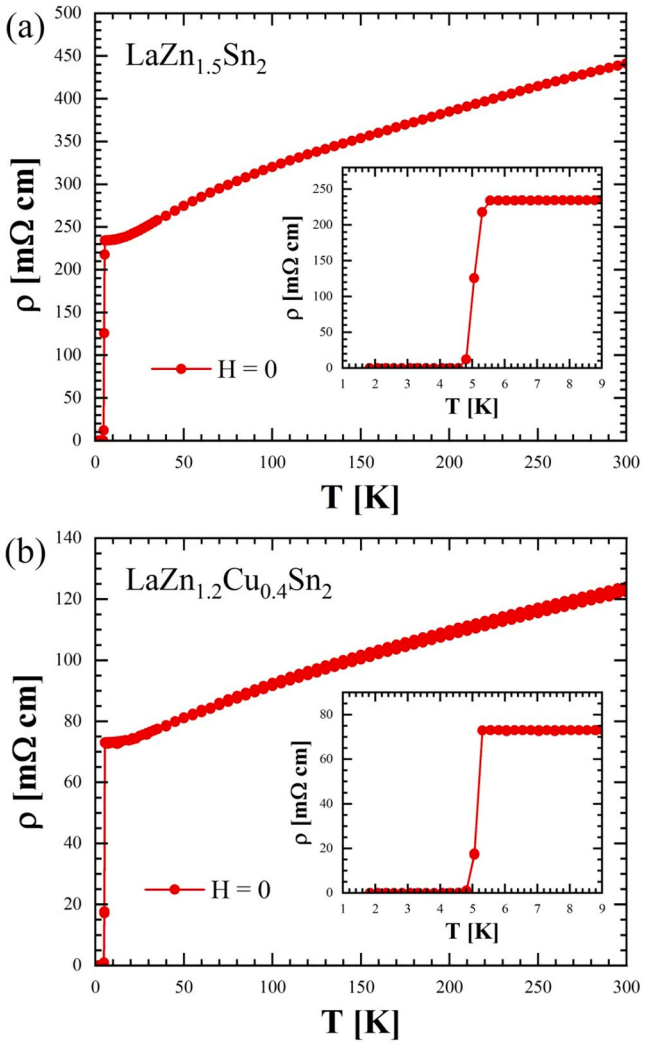

Fig. 10. Zero-field electrical resistivity for $LaZn_{1.5}Sn_2$ (a) and $LaZn_{1.2}Cu_{0.4}Sn_2$ (b) measured between 1.8 K and 300 K.

Zn distances along the *a* axis [2.7907(8) Å *vs.* 3.5471(9) Å]. It shall also be noted that octahedra vertices exhibit just 90% occupation, thus causing positional disorder of the neighboring Sn sites from the pyramidal vertices.

Finally, in the $La(Zn,T)_{2-x}Sn_2$ compounds formed by the larger

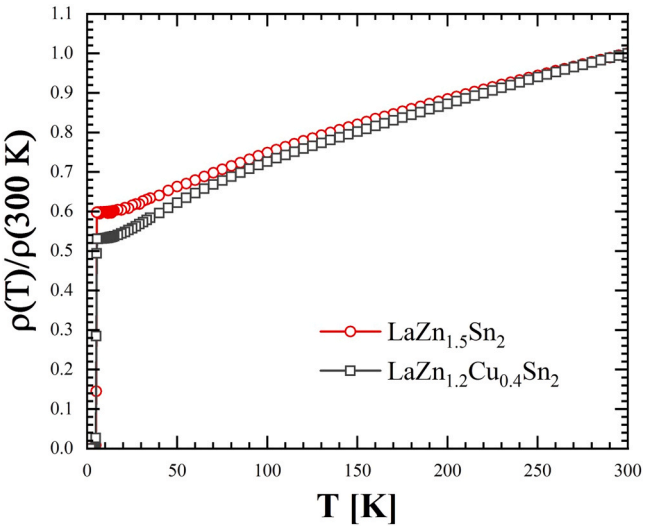

Fig. 11. A comparison between the zero-field temperature-dependent electrical resistivity, normalized to the value at T = 300 K, [ρ(T)/ρ(300 K)], of the $LaZn_{1.5}Sn_2$ and $LaZn_{1.2}Cu_{0.4}Sn_2$ compounds.

transition metals (*i.e.*, Ti, Ag, Cd and Au), the existence of two further related structures has been observed. These compounds crystallize with a practically doubled unit cell compared to that of the orthorhombic $LaZn_{1.445(2)}Sn_2$ (the longest cell parameter is doubled and the two others are basically unaffected). The refined atomic coordinates and crystal structure details are collected in Tables S10 for $LaZn_{1.099(4)}Ag_{0.36(1)}Sn_{2.00(1)}$ [own prototype, *oC*108−x (x = 36); indicated as $LaZn_{1.1}Ag_{0.4}Sn_2$-type from here on], Table S11 for $LaZn_{1.15(1)}Ti_{0.42(1)}Sn_{2.00(1)}$ [$LaZn_{1.1}Ag_{0.4}Sn_2$-type, *oC*108−x (x = 34.936)], Table S12 for $LaZn_{1.323(7)}Cd_{0.17(2)}Sn_{2.014(3)}$ ($LaZn_{1.1}Ag_{0.4}Sn_2$-type, *oC*108−x (x = 35.884)] and Table S13 for $LaZn_{1.360(3)}Au_{0.269(7)}Sn_{2.01(2)}$ (own prototype, *oC*112−x (x = 37.748)]. The lattice parameters for all these phases are reported in Table 3.

For $LaZn_{1.15(1)}Au_{0.42(1)}Sn_{2.00(1)}$, $LaZn_{1.099(4)}Ag_{0.36(1)}Sn_{2.00(1)}$ and $LaZn_{1.323(7)}Cd_{0.17(2)}Sn_{2.014(3)}$ the unit cell involves four Wyckoff sites fully occupied by La atoms (with 4*j* and 4*i* symmetry). While in $LaZn_{1.15(1)}Au_{0.42(1)}Sn_{2.00(1)}$ there are three Wyckoff sites for Zn atoms (one with 16*r* symmetry fully occupied, one with 4*i* symmetry partially vacant and one with 4*i* symmetry statistically filled by Zn/Ti), for $LaZn_{1.099(4)}Ag_{0.36(1)}Sn_{2.00(1)}$ and $LaZn_{1.323(7)}Cd_{0.17(2)}Sn_{2.014(3)}$ there are four atomic positions for Zn atoms (one of them with 16*r* symmetry, two with 4*i* symmetry and one with 4*j* symmetry; among them only one with 4*i* symmetry is fully occupied). In both $LaZn_{1.099(4)}Ag_{0.36(1)}Sn_{2.00(1)}$ and

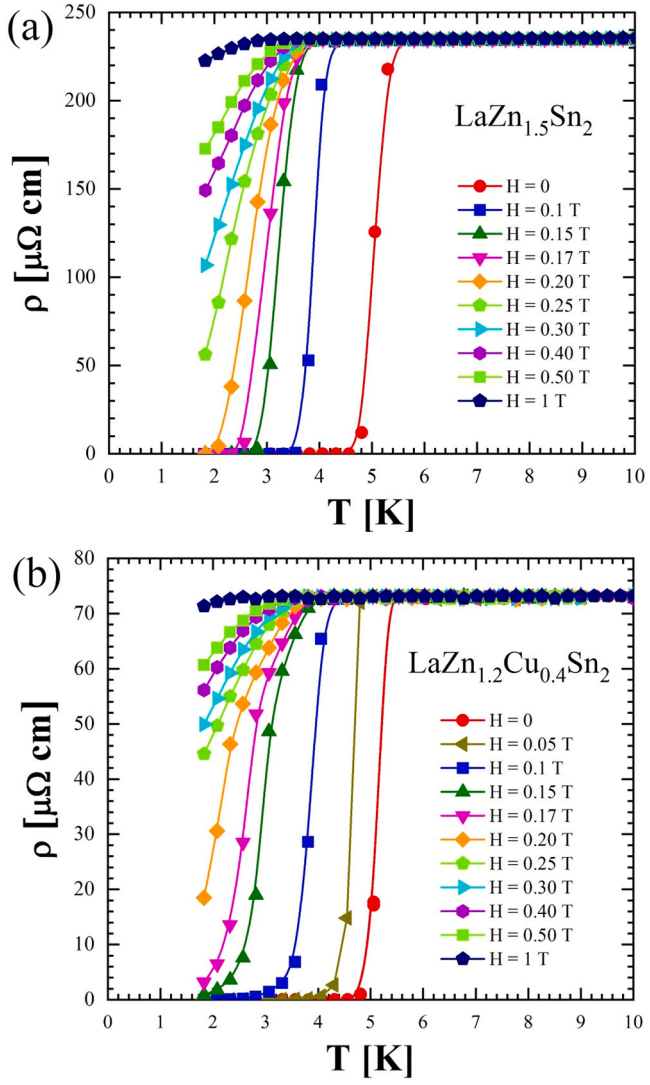

Fig. 12. In field-electrical resistivity for $LaZn_{1.5}Sn_2$ (a) and $LaZn_{1.18}Cu_{0.36}Sn_2$ (b) measured between 1.8 K and 300 K.

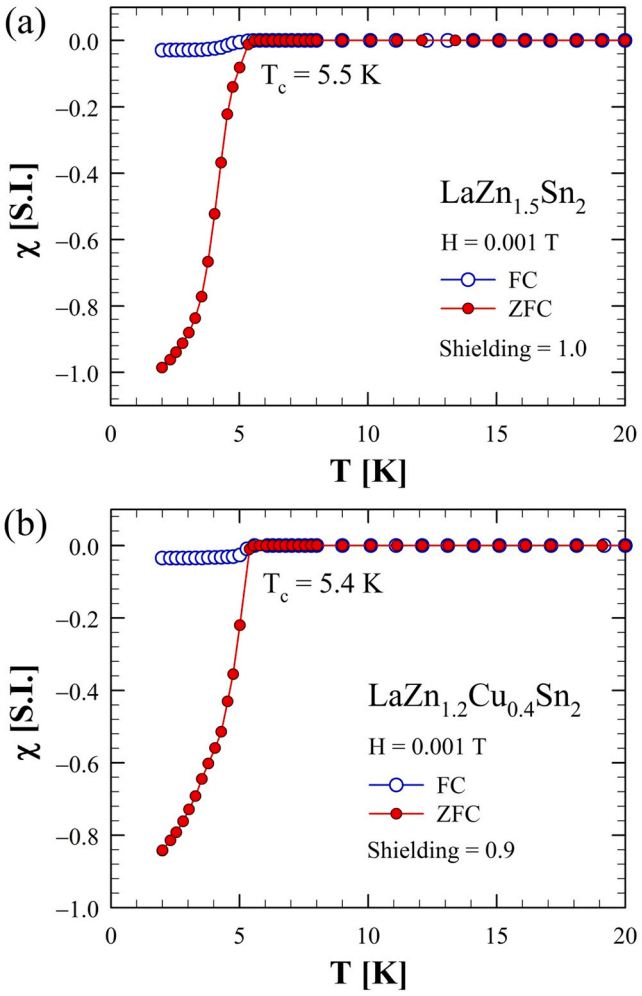

Fig. 14. Magnetic susceptibility *vs.* temperature for $LaZn_{1.5}Sn_2$ (a) and $LaZn_{1.2}Cu_{0.4}Sn_2$ (b) compounds measured between 1.8 K and 20 K and in the applied magnetic field of 0.001 T.

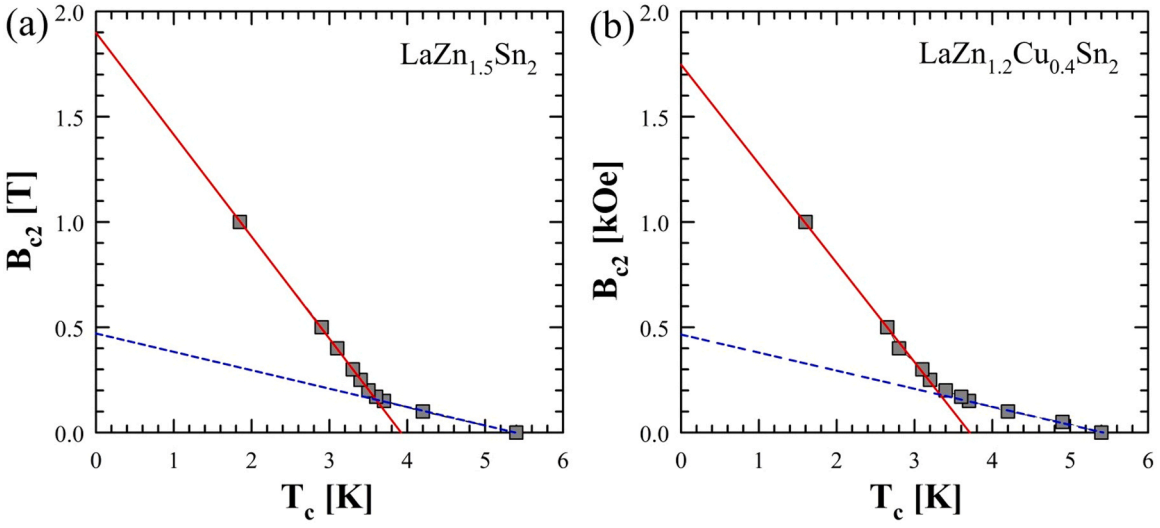

Fig. 13. Graph of the linear extrapolation of the upper critical field, B_{c2} (as deduced from the resistivity data) *vs.* the temperature for $LaZn_{1.5}Sn_2$ (a) and $LaZn_{1.2}Cu_{0.4}Sn_2$ (b).

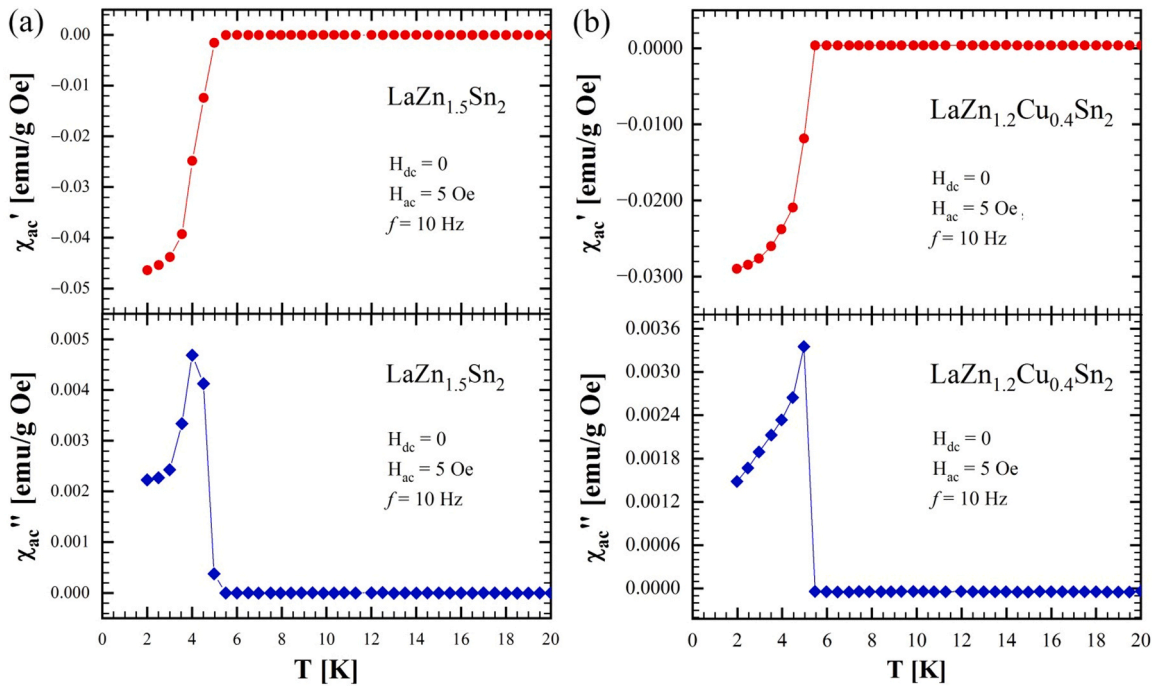

Fig. 15. The *ac* magnetic susceptibility data *vs.* temperature up to 20 K for $LaZn_{1.5}Sn_2$ (a) and $LaZn_{1.2}Cu_{0.4}Sn_2$ (b); the real χ_{ac}' and imaginary χ_{ac}'' components are shown in the upper and lower plot, respectively.

$LaZn_{1.323(7)}Cd_{0.17(2)}Sn_{2.014(3)}$, one only atomic site (16*r*) is partially occupied by either Ag or Cd atoms, while it was found that Ti atoms occupy two different 4*j* sites (one being partially vacant and the other containing both Ti and Zn) in $LaZn_{1.15(1)}Ti_{0.42(1)}Sn_{2.00(1)}$. In all the three compounds, ten Wyckoff sites are occupied by Sn atoms [two of them being fully occupied (8*o* and 8 *m*), and all the others being partially vacant (4*i* and 4*j*)] (Table S10, Table S11 and Table S12). For $LaZn_{1.360(3)}Au_{0.269(7)}Sn_{2.01(2)}$, the unit cell also involves four fully occupied atomic positions for La atoms (with 4*j* and 4*i* symmetry), four Wyckoff sites for Zn atoms (two of them, with 16*r* and 4*i* symmetry being partially vacant and two of them, with 4*i* and 4*j* symmetry being fully occupied), one atomic site (16*r*) partially occupied by Au atoms and eleven atomic positions for Sn atoms [four with 4*i* symmetry (all partially occupied)], five with 4*j* symmetry (all partially occupied), one with 8*o* symmetry and one with 8 *m* symmetry (these two fully occupied) (Table S13).

The structure of these compounds exhibits motifs identical to those in the orthorhombic $LaZn_{1.445(2)}Sn_2$, but in different proportions; three pyramidal layers and one octahedral, as demonstrated for the case of $LaZn_{1.10(1)}Ag_{0.36(1)}Sn_2$ (Fig. 9). The connectivity mechanisms and consequently disorders are very similar to $LaZn_{1.445(2)}Sn_2$, involving major parts of the polyanionic net. Octahedral layers (O) represent certain islands of stability exhibiting no disorder together with the rectangular tiling of the P* layers (Fig. 9). Rectangular tiling of the P layers exhibits minor occupational disorder expressed in Zn/Ag mixing. All remaining Zn and Sn sites are positionally disordered showing a high degree of correlation between the neighboring layers. Pyramidal vertices of the neighboring layers are always oriented toward each other, while the pyramids having direct contacts with the octahedra are also squashed in analogy to $LaZn_{1.445(2)}Sn_2$. A similar unit cell has also been detected with Cr, although no good-quality crystals could be found for a detailed structural characterization.

3.3. Physical properties

The physical properties (electrical resistivity, magnetic susceptibility and heat capacity) have been measured for $LaZn_{1.5}Sn_2$ and the substituted $LaZn_{1.2}Cu_{0.4}Sn_2$ compounds. The zero-field and in-field electrical resistivity between 2 and 300 K are shown in Figs. 10**a** and **b**, respectively. The data show for both compounds a typical metallic behavior ($d\rho/dT > 0$), with the resistivity decreasing while decreasing the temperature from 300 K down to about 6 K. As the temperature is decreased, a sharp drop in the resistivity occurs at 5.5 K for $LaZn_{1.5}Sn_2$ and at 5.4 K for $LaZn_{1.2}Cu_{0.4}Sn_2$, confirming the transition to a superconducting state. Zero resistivity is attained at 4.8 K for the former and at 4.6 K for the latter indicating the transition to occur in a very narrow temperature range of 0.5 K. Though the two compounds show comparable T_cs, the Cu substituted compound shows a resistivity which is about 200 μΩ cm lower than that of the pristine compound, while one would have expected that Cu substitution should have increased the electrical resistivity as it contributes to increase the crystallographic disorder. However, as the overall electrical resistivity behavior of the two compounds [plotted as normalized resistivity, ρ(T)/ρ(300 K) in Fig. 11] appears to be very similar, we attribute the aforementioned difference mainly due to the determination of the geometric factor of the specimens used for the measurement. The electrical resistivity for the two compounds, measured under several applied magnetic fields and between 1.8 and 10 K, is then shown in Figs. 12**a** and **b**, respectively. As the magnetic field increases, T_c gradually decreases. The values of the upper critical magnetic field, B_{c2}, are evaluated at the onset of the resistivity transition, by intercepting the resitivity curves with the horizontal line $\rho_N \times 0,95$, where ρ_N is the resistivity value evalutated above the transition. B_{c2} increases with decreasing temperature exhibiting for both $LaZn_{1.5}Sn_2$ and $LaZn_{1.2}Cu_{0.4}Sn_2$ compounds (Figs. 13**a** and **b**, respectively) a very similar temperature behavior. Starting from $B_{c2} = 0$ at $T_c = 5.5$ K, B_{c2} linearly increases with decreasing temperature, and at $T \approx 3.5$ K, the slope suddenly increases. For both the samples, a value of 10 T is achieved at 2 K. This behavior suggests the presence of two superconducting phases, likely coexisting in the samples and with different T_c, that we think to be corresponding to the tetragonal (the predominant and likely forming at higher temperature; phase I) and the orthorhombic (the secondary and likely forming at a lower temperature; phase II) forms. In order to characterize the two phases, the linear behaviors occurring between 3.5 and 5.5 K and between 2 K and 3.5 K are

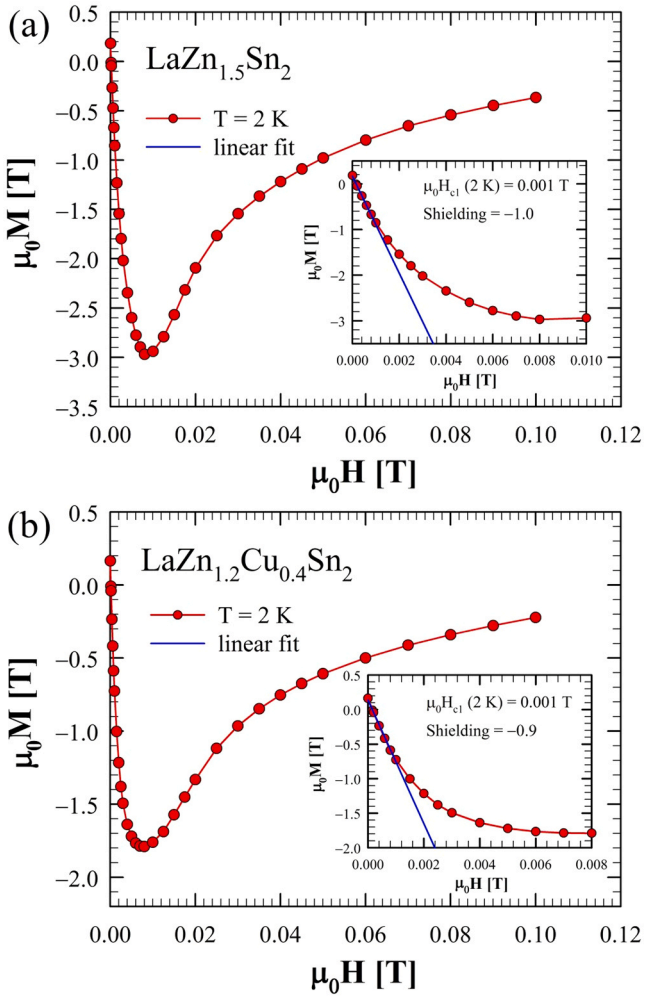

Fig. 16. Isothermal magnetization at T = 2 K measured up to H = 0.1 T for $LaZn_{1.5}Sn_2$ (a) and $LaZn_{1.2}Cu_{0.4}Sn_2$ (b).

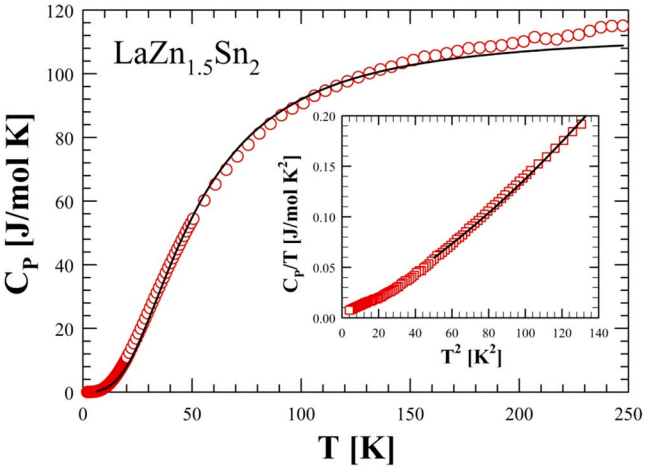

Fig. 17. Zero-field specific heat, C_P, as a function of temperature between 2 K and 250 K for $LaZn_{1.5}Sn_2$. The solid line is a fit obtained by using the Debye model. The inset shows C_P/T *vs.* T^2 data up to nearly 12 K. The solid line is a fit to the data between 7 and 12 K using the expression described in the text.

best fitted, as shown in Figs. 13**a** and 13**b**. For the $LaZn_{1.5}Sn_2$ compound the estrapolation of B_{c2} to zero provides the evaluation of T_c, which is 5.5 K for the high temperature phase (phase I) and 3.9 K for the low

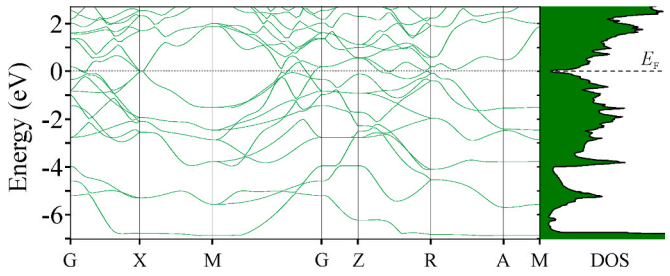

Fig. 18. Electronic band structure and total DOS of $LaZn_{1.5}Sn_2$ between −7 and 3 eV.

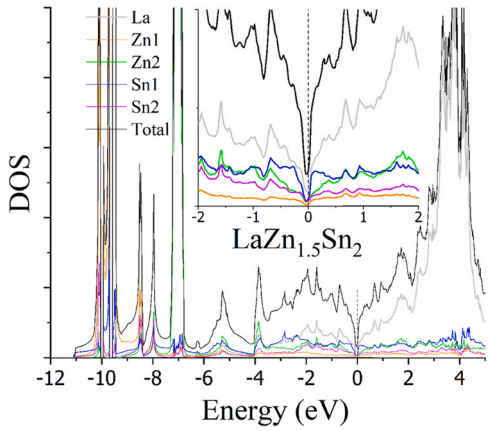

Fig. 19. Element-projected and total densities of states in $LaZn_{1.5}Sn_2$.

temperature phase (phase II). An uppermost evaluation of $B_{c2}(0)$ can be given assuming the Werthamer-Helfand-Hohenberg (WHH) theory [39] in the dirty limit $B_{c2}(0) = 0.7 \frac{dB_{c2}}{dT} T_c$. So we obtain $B_{c2}(0) = 0.34$ T for the phase I and $B_{c2}(0) = 1.3$ T for the phase II. Very similar values of T_c and $B_{c2}(0)$ of the two phases are evaluated for the $LaZn_{1.2}Cu_{0.4}Sn_2$ compound. So we can conclude that Cu presence does not affect the coexistence of the two phases, nor does it modify their superconducting properties. From the $B_{c2}(0)$ values, using the relationship $B_{c2} = \frac{\phi_0}{(2\pi\xi^2)}$, the coherence lengths of the two phases can be evaluated, which come out, respectively, $\xi_I = 27$ nm and $\xi_{II} = 16$ nm.

The temperature dependence of the zero-field-cooled (ZFC) and field-cooled (FC) DC magnetic susceptibility, $\chi_{dc}(T)$, measured under applied magnetic fields of 1 mT, in between 2 and 20 K, is shown in Figs. 14**a** and **b** for $LaZn_{1.5}Sn_2$ and $LaZn_{1.2}Cu_{0.4}Sn$, respectively. The ZFC $\chi_{dc}(T)$ data reveal the presence of a total field shielding, suggesting the appearance of bulk superconductivity transition with temperature $T_c^{onset} \approx 5.5$ K for both compounds. This result further suggests this Tc to pertain to the predominant phase I. In order to emphasize the contribution of the low temperature phase II, the derivative $\chi_{dc}(T)$ is plotted as a dashed line in Figs. 14**a** and **b**. Interestingly, the $LaZn_{1.2}Cu_{0.4}Sn$ curve exhibits two peaks. The low temperature peak appears at 3.5 K which is just below the transition temperature of the phase II evaluated by B_{c2} analysis. Looking at the ZFC $\chi_{dc}(T)$ curve, at 3.5 K a feature corresponding to a double transition can be envisaged and by the value of ZFC $\chi_{dc}(T)$ at 3.5 K we can infer that the two phases contribute approximately equally to shielding. The $LaZn_{1.5}Sn_2$ derivative shows a single peak at 4 K, corresponding to a change of slope in the ZFC $\chi_{dc}(T)$. This behavior does not rule out contributions from both phases, although these may not be separable. The AC magnetic susceptibility data including both the real part, χ_{ac}', and the imaginary part, χ_{ac}'', measured at 10 Hz frequency, are shown in Figs. 15**a** **b** for $LaZn_{1.5}Sn_2$ and $LaZn_{1.2}Cu_{0.4}Sn_2$, respectively. Both the real (χ_{ac}') and imaginary (χ_{ac}'') parts

confirm superconductivity in terms of a diamagnetic transition in χ_{ac}' and a peak seen in χ_{ac}'' [40,41]. The temperature resolution of the measurements, acquired at one point every 0.5 K, does not allow for the separation of the two phases. The superconducting nature is further corroborated by isothermal magnetization data, M(H), measured at T = 2 K, in the superconducting state, for $LaZn_{1.5}Sn_2$ and $LaZn_{1.2}Cu_{0.4}Sn_2$ (Figs. 16**a** and **b**, respectively). The magnetization linearly decreases with a slope which is close to −1 as the field increases up to $B_{c1} = 10$ mT for both compounds, indicating a perfect diamagnetic character for both of them. While the applied field increases, above the magnetic field B_{c1}, the absolute value of magnetization stops increasing linearly and progressively starts decreasing up to tending to zero. The M(H) was measured up to 0,1 T; however, the upper critical field, B_{c2}, estimated from electrical resistivity measurements (Figs. 13**a** and **b**) is as high as 0, 43 T and 1.3 T for tetragonal phase I and orthorhombic phase II, respectively. These magnetization curves would apparently indicate a type-II nature of the superconductivity for $LaZn_{1.5}Sn_2$ and $LaZn_{1.2}Cu_{0.4}Sn_2$. From the $B_{c1} \approx 10$ mT value, it is possible evaluate the London penetration depth, λ, from the equation $B_{c1} = \frac{\phi_0}{4\pi\lambda^2}\left(\ln\frac{\lambda}{\xi} + 0.497\right)$. For the calculation of λ, it is necessary to attribute H_{c1} to one of the two phases (ξ is different in the two phases). Because it represents the field at which the fluxons start penetrating the samples, it can reasonbly be attributed to phase I, having lower B_{c2}. With this assumption we evauate $\lambda_I \approx 0,14\ \mu m$. A bit higher value, $\lambda_{II} \approx 0,15\ \mu m$, is obtained attributing B_{c1} to phase II. Finally Ginzburg-Landau parameter $\kappa = \frac{\lambda}{\xi}$ can be calculated for both the phases: $\kappa_I = 5$ and $\kappa_{II} = 10$.

The heat capacity, C_P, of $LaZn_{1.5}Sn_2$ was measured in the temperature range of 2–250 K (Fig. 17). Unexpectedly, the data show practically no jump (ΔC_P) around T_c [42]. From first glance, the absence of a jump in C_P is not consistent with the robust and reproducible jump of electrical resistivity to zero and with the strong diamagnetic signal observed in the magnetization data (Figs. 10**a** and 14**a**). Taking into attention the extensive positional disorder observed in certain parts of the structure, in particular extensive cavities filled by Sn2–4 positions (see Fig. 3), one may not exclude that the heat during the transition would partially be transferred into multiple and minor positional changes in the structure able to hind the jump. It is also worth noting that in the compositionally related La_2Sn_3 the jump in specific heat is also hardly visible, as spread out over a wider region which makes it very difficult to observe [43]. However, we believe that the presence of two phases with different T_c values, each contributing approximately equally to the total volume as inferred by the analisys of electrical and magnetic measurements, may explain why the peak was not observed. According to the BCS model of superconductivity in the weak coupling limit, the jump, ΔC_P, at T_c is 1.43 γT_c, where γ is the Sommerfeld coefficient of the heat capacity due to the electronic density of the states at the Fermi level. Normally, γ is determined by fitting the expression $C_P/T = \gamma + \beta T^2$ to the data at low temperatures, where β is the coefficient of the lattice heat capacity. We cannot apply this method for the data below 6 K as the sample is in the superconducting state. In the absence of data in applied magnetic field exceeding the upper critical field H_{c2} such that the superconductivity is destroyed and the sample is in the normal state, we have fitted the modified Debye expression $C_P/T = \gamma + \beta T^2 + \delta T^4$ to the normal state data between 7 and 12 K, above T_c. The last term was added as there is a slight curvature in the C_P/T *vs.* T^2 plot (inset Fig. 17). The values of the fitted coefficients are $\gamma = 0.37$ mJ/mol K^2, $\beta = 0.9821$ mJ/mol K^4 and $\delta = 3.9014 \times 10^{-3}$ mJ/mol K^6. The Debye temperature, Θ_D, calculated using the equation $\Theta_D = \left(\frac{12\pi^4}{5\beta}nR\right)^{1/3}$, where β is in J/g atom K^4, was found to be 207 K. We have also fitted the following expression to the heat capacity data between 6 and 250 K, after the electronic contribution γT was subtracted from the total heat capacity:

$$C_{\text{Debye}} = 9nR\left(\frac{T}{\Theta_D}\right)^3 \int_0^{\frac{\Theta_D}{T}} \frac{x^4 e^x}{(e^x-1)^2} dx$$

The equation provides a fairly good fit to the data with $\Theta_D = 205$ K. Some deviation is seen at higher temperatures. It may be noted that the values of Θ_D obtained from the two different methods described above are nearly matching.

Other compounds have also been surveyed by means of the magnetization measurements to investigate the influence of multiple factors on the superconducting behavior. Several of the La compounds reveal superconducting transitions in the temperature range of ≈ 5.0–4.0 K. The transition temperature, T_c, has been found to show a certain correlation with the nature and amount of the dopants. For instance, the T_c of Cu-richer $LaZnCu_{0.8}Sn_2$ is 5.05 K, while it drops to 4.2 K for the Pd and Pt substituted homologues $LaZn_{1.1}Pd_{0.4}Sn_2$ and $LaZn_{1.0}Pt_{0.5}Sn_2$ (Figure S2 **for** $LaZn_{1.0}Pt_{0.5}Sn_2$); this may be related to the degree of disorder. Compounds containing a magnetic atom, such as $LaZn_{1.1}Mn_{0.4}Sn_2$ and $LaZn_{1.2}Ni_{0.4}Sn_2$, did not show any superconductivity. While even orthorhombic $LaZn_{1.44}Sn_2$ seems to be a superconductor (with a slightly lower $T_c = 5.0$–5.2 K), no superconductivity has been observed in the other orthorhombic phases $LaZn_{1.1}Ag_{0.4}Sn_2$, $LaZn_{1.3}Cd_{0.2}Sn_2$ and $LaZn_{1.4}Au_{0.3}Sn_2$ (see Tables S9-S12 for structural details on these orthorhombic phases). More work is underway to confirm the superconducting properties of the ternary orthorhombic $LaZn_{1.44}Sn_2$ and to further investigate the formation, range of compositional existence, thermodynamic stability, crystal structure and physical properties of these new pseudo-ternary compounds formed with other R and *T* elements.

3.4. Electronic structure

Electronic structure calculations have been performed for an idealized stoichiometric composition $LaZn_2Sn_2$ while the Fermi level has been adjusted for the observed valence electron count of 14 e^- (Figs. 18 and 19). The electronic density of states (DOS) curves are characterized by broad *s* and *p* bands extending ≈ 11 eV below the Fermi level and sharp large bands of Zn dominating below −7 eV. The contributions from all elements are nearly equal approaching the Fermi level, where those from La start to dominate. Non-zero values at the Fermi level suggest poor metallic characteristic that is quite predictable and matches with the resistivity measurements. It is not unexpected that a narrow and deep pseudogap has been observed at the *vec* = 14 e^- as it is a common optimum value (magic number of valence electrons) for $BaAl_4$-type and its derivatives [44–46]. Multiple van Hove singularities have been observed around high symmetry points, particularly Z and R, 0.01–0.1 eV below the Fermi level being consistent with the observed superconducting behavior [47]. Additionally, the feature around the X point is reminiscent of a Dirac cone; however, it is accompanied by short flat bands in the X-M direction right above and below the Fermi level.

4. Conclusions

The new compound $LaZn_{2-x}Sn_2$ has been identified and investigated. It crystallizes in a disordered structure, derivative of the tetragonal $CaBe_2Ge_2$-type, with the stoichiometry of $LaZn_{1.5}Sn_2$ and almost no solid solubility. The $RZn_{2-x}Sn_2$ intermetallic also exists for the other light rare earth elements (R = Ce-Nd) but Sm. Within the $RZn_{2-x}Sn_2$ family, ongoing from the larger La to the smaller Nd, the atomic fraction of Zn in the unit cell decreases from 1.5 to 1.3; this effect is likely due to the lanthanide contraction, which concomitantly leads to a decrease of the overall unit cell volume. DTA analysis indicates these phases form by a peritectic reaction competing with the formation of the congruently melting RZn_xSn_{3-x}. $LaZn_{1.5}Sn_2$ was found to be a superconductor at $T_c =$ 5.5 K; therefore we investigated the pseudoternary $La(Zn,T)_{2-x}Sn_2$ phases with partial substitution of Zn by a transition metal *T*, to check

for the effects on superconductivity. We found these phases to exist for a large number of transition metals (T = Ti, Mn, Fe, Co, Ni, Cu, Pd, Ag, Cd, Pt, Au) and x ≈ 0.4–0.5. The magnetic susceptibility, electrical resistivity and heat capacity have been measured for $LaZn_{1.5}Sn_2$ and the Cu-substituted $LaZn_{1.2}Cu_{0.4}Sn_2$. Altogether, these data confirm the superconducting transition in these two materials to occur at $T_c = 5.5$ K in $LaZn_{1.5}Sn_2$ and $T_c = 5.4$ K in $LaZn_{1.2}Cu_{0.4}Sn_2$.

The susceptibility measurements confirm the superconductivity is preserved in $La(Zn,T)_{2-x}Sn_2$ compounds (T = Cu, Pd and Pt) crystallizing in the tetragonal crystal structure, but not in the $RZn_{2-x}Sn_2$ compounds formed by a magnetic R, in $La(Zn,T)_{2-x}Sn_2$ with T = Mn, Ni, nor in $La(Zn,T)_{2-x}Sn_2$ with T = Ag, Au and Cd, crystallizing in new orthorhombic derivative superstructures of the orthorhombic $LaZn_{2-x}Sn_2$.

The parameters leading to the formation of the ternary orthorhombic $LaZn_{1.44}Sn_2$, *i.e.*: local Zn concentration in the melt linked to the cooling rate, or a low-temperature form needing a lower and long annealing temperature, remain to be further investigated. Even orthorhombic $LaZn_{1.44}Sn_2$ seems to be a superconductor, with a T_c slightly lower (5.0–5.2 K) with respect that of the tetragonal structure; however, further work is underway to confirm or disprove the superconducting properties of this ternary orthorhombic compound.

The presence of superconductivity in a heavily disordered compound such as $LaZn_{1.5}Sn_2$ is somewhat unexpected and is followed by another unexpected observation, a negligible ΔC_P jump that apparently is incompatible with the robust and reproducible diamagnetic response observed. Such ΔC_P response may in part be attributed to the presence of impurities and/or the same occupational disorder allowing extensive positional freedom of certain sites.

These compounds represent a new group of superconductors where the superconducting properties may be properly tuned by varying the chemical (atomic substitutions) and/or physical (pressure) parameters. A more detailed investigation of these phases is currently underway trying to shed light on the relationships between these complex disordered crystal structures and the appearance of superconductivity, in an attempt to predict this phenomenon for new materials suitable for potential technological applications.

CRediT authorship contribution statement

Volodymyr Smetana: Writing – review & editing, Writing – original draft, Validation, Methodology, Investigation, Formal analysis, Data curation. **Vitalii Shtender:** Investigation, Formal analysis. **Stefanie Siebeneichler:** Formal analysis. **Marina Putti:** Writing – review & editing, Validation, Methodology, Formal analysis. **Alexandra Franz:** Formal analysis. **Carlo Ferdeghini:** Validation. **Vitalij K. Pecharsky:** Validation, Supervision, Investigation, Formal analysis, Data curation. **Anja-Verena Mudring:** Writing – original draft, Validation, Data curation, Supervision, Project administration, Funding acquisition. **Pietro Manfrinetti:** Writing – review & editing, Writing – original draft, Validation, Supervision, Project administration, Methodology, Investigation, Funding acquisition, Formal analysis, Data curation. **Alessia Provino:** Writing – review & editing, Writing – original draft, Validation, Supervision, Methodology, Investigation, Formal analysis, Data curation.

Declaration of Competing Interest

The authors declare that they have no known competing financial interests or personal relationships that could have appeared to influence the work reported in this paper.

Data Availability

Data will be made available on request.

Acknowledgments

P. Manfrinetti is grateful for funding granted by Compagnia San Paolo through the scientific project entitled “Nitride compounds: new superconductors from a still little-investigated world” (2017–2019). A. Provino and P. Manfrinetti would like to thank the project NEWS that has supported their stay at the Ames Laboratory in 2018. Work at Ames Laboratory is supported by the U.S. Department of Energy, Office of Basic Energy Sciences, Materials Sciences Division. The Ames Laboratory is operated for the U. S. Department of Energy by Iowa State University of Science and Technology under contract No. DE-AC02-07CH11358. Authors acknowledge the neutron source BER II, Helmholtz-Zentrum Berlin für Materialien und Energie, Berlin, Germany for experiments performed in this facility (proposal No. 18207551). Stefanie Siebeneichler is funded by the Swedish Foundation for Strategic Research (SSF), within the Swedish national graduate school in neutron scattering (SwedNess). Research at Aarhus University was supported by the DFF through grant no. 2102-00143B. Authors are also grateful to Professors S. K. Dhar and A. Thamizhavel (TIFR, Mumbai, India) for the help received in performing most of the heat capacity measurements.

Appendix A. Supporting information

Supplementary data associated with this article can be found in the online version at doi:10.1016/j.jallcom.2024.175025.

References

[1] J. Bardeen, L.N. Cooper, J.R. Schrieffer, Theory of superconductivity, Phys. Rev. 108 (1957) 1175–1204, https://doi.org/10.1103/PhysRev.108.1175.
[2] R.A. Hawsey, S. Morozumi, The energy and environmental benefits of superconducting power products, Mitig. Adapt. Strateg. Glob. Chang. 10 (2005) 279–306, https://doi.org/10.1007/s11027-005-9031-4.
[3] S. Ghosh, A. Shekhter, F. Jerzembeck, N. Kikugawa, D.A. Sokolov, M. Brando, A. P. Mackenzie, C.W. Hicks, B.J. Ramshaw, Thermodynamic evidence for a two-component superconducting order parameter in Sr_2RuO_4, Nat. Phys. 17 (2021) 199–204, https://doi.org/10.1038/s41567-020-1032-4.
[4] Y. Kamihara, H. Hiramatsu, M. Hirano, R. Kawamura, H. Yanagi, T. Kamiya, H. Hosono, Iron-based layered superconductor: LaOFeP, J. Am. Chem. Soc. 128 (2006) 10012–10013, https://doi.org/10.1021/ja063355c.
[5] D. Lin, H.-S. Xu, J. Luo, H. Huang, Y. Lu, K. Tang, A self-doped oxygen-free high-critical-temperature (High-Tc) superconductor: SmFFeAs, Inorg. Chem. 58 (2019) 15401–15409, https://doi.org/10.1021/acs.inorgchem.9b02464.
[6] M.C. Diamantini, C.A. Trugenberger, V.M. Vinokur, Topological nature of high temperature superconductivity, Adv. Quantum Technol. 4 (2021) 2000135, https://doi.org/10.1002/qute.202000135.
[7] B.T. Matthias, T.H. Geballe, R.H. Willens, E. Corenzwit, G.W. Hull, Superconductivity of Nb_3Ge, Phys. Rev. 139 (1965) A1501–A1503, https://doi.org/10.1103/PhysRev.139.A1501.
[8] H. Takahashi, K. Igawa, K. Arii, Y. Kamihara, M. Hirano, H. Hosono, Superconductivity at 43 K in an iron-based layered compound $LaO_{1-x}F_xFeAs$, Nature 453 (2008) 376–378, https://doi.org/10.1038/nature06972.
[9] M.A. Rahman, M.Z. Rahaman, M.N. Samsuddoha, A review on cuprate based superconducting materials including characteristics and applications, AJPA 3 (2015) 39–56, https://doi.org/10.11648/j.ajpa.20150302.15.
[10] I. Oshchapovsky, V. Pavlyuk, Systems {La, Tb}–Zn–{Sn, Pb}, Visnyk of the Lviv University, Ser. Chem. 56 (2015) 53–61, https://doi.org/http://publications.lnu.edu.ua/bulletins/index.php/chemisrty/article/view/6317/6324.
[11] P. Manfrinetti, M. Pani, RZnSn (R=rare earth): a novel series of intermetallic compounds with the YPtAs structure type, J. Alloy. Compd. 393 (2005) 180–184, https://doi.org/10.1016/j.jallcom.2004.10.010.
[12] N.-T. Suen, S. Bobev, Synthesis and structural characterization of $RE_7Zn_{21}Tt_2$ (RE = La–Nd; Tt = Ge, Sn, and Pb): new structure type among the polar intermetallic phases, Inorg. Chem. 52 (2013) 12731–12740, https://doi.org/10.1021/ic4019844.
[13] N.-T. Suen, S. Bobev, New polar intermetallic phases RE_2Zn_5Tt (RE = La–Nd; Tt = Sn and Pb): synthesis, structure, chemical bonding, and magnetic properties, Inorg. Chem. 52 (2013) 9102–9110, https://doi.org/10.1021/ic401339v.
[14] E. Parthe, B. Chabot, H.F. Braun, N. Engel, Ternary $BaAl_4$-type derivative structures, Acta Crystallogr. Sect. B 39 (1983) 588–595, https://doi.org/10.1107/S010876818300302X.
[15] J. Leciejewicz, S. Siek, A. Szytuła, Structural properties of ThT_2Si_2 compounds, J. Less Common Met. 144 (1988) L9–L13, https://doi.org/10.1016/0022-5088(88)90150-6.
[16] B. Eisenmann, N. May, W. Müller, H. Schäfer, Eine neue strukturelle variante des $BaAl_4$-typs: Der $CaBe_2Ge_2$-Typ / a new structural variant of the $BaAl_4$-type: the

$CaBe_2Ge_2$-type, Z. Naturforsch. B 27 (1972) 1155–1157, https://doi.org/10.1515/znb-1972-1008.
[17] M. Rotter, M. Tegel, D. Johrendt, Superconductivity at 38 K in the Iron Arsenide $Ba_{1-x}K_xFe_2As_2$, Phys. Rev. Lett. 101 (2008) 107006, https://doi.org/10.1103/PhysRevLett.101.107006.
[18] S. Ganesanpotti, T. Yajima, T. Tohyama, Z. Li, K. Nakano, Y. Nozaki, C. Tassel, Y. Kobayashi, H. Kageyama, $LaPd_2Sb_2$: a pnictide superconductor with $CaBe_2Ge_2$ type structure, J. Alloy. Compd. 583 (2014) 151–154, https://doi.org/10.1016/j.jallcom.2013.08.005.
[19] Q. Mu, B. Pan, B. Ruan, T. Liu, K. Zhao, L. Shan, G. Chen, Z. Ren, Superconductivity in $LaPd_2Bi_2$ with $CaBe_2Ge_2$-type structure, Sci. China.: Phys. Mech. Astron. 61 (2018) 127409, https://doi.org/10.1007/s11433-018-9285-5.
[20] K. Kudo, Y. Nishikubo, M. Nohara, Coexistence of superconductivity and charge density wave in $SrPt_2As_2$, J. Phys. Soc. Jpn. 79 (2010) 123710, https://doi.org/10.1143/JPSJ.79.123710.
[21] Y. Nakayama, T. Muranaka, Superconductivity in $LaRh_2Ga_2$ with noncentrosymmetric structure, Inorg. Chem. 58 (2019) 12733–12738, https://doi.org/10.1021/acs.inorgchem.9b01342.
[22] W. Xie, E.M. Seibel, R.J. Cava, The new superconductor tP-$SrPd_2Bi_2$: structural polymorphism and superconductivity in intermetallics, Inorg. Chem. 55 (2016) 3203–3205, https://doi.org/10.1021/acs.inorgchem.5b02900.
[23] J. Liang, Y. Han, Y. Ouyang, S. Xie, J. Meng, L. Zhu, M. Ling, Experimental investigation on phase equilibria of Ce-Sn-Zn system at 400 °C, J. Rare Earth 30 (2012) 916–922, https://doi.org/10.1016/S1002-0721(12)60154-9.
[24] S.K. Dhar, P. Paulose, R. Kulkarni, P. Manfrinetti, M. Pani, N. Parodi, Crystal structure and magnetic ordering in dimorphic $EuZn_2Sn_2$, Solid State Commun. 149 (2009) 68–72, https://doi.org/10.1016/j.ssc.2008.10.014.
[25] R. Pöttgen, J.H. Albering, D. Kaczorowski, W. Jeitschko, Structure refinements of actinoid transition metal stannides $AnT_{2-x}Sn_{2-y}$ (An = Th, U; T = Co, Ni, Cu) with defect $CaBe_2Ge_2$-type structure, J. Alloy. Compd. 196 (1993) 111–115, https://doi.org/10.1016/0925-8388(93)90579-C.
[26] A. Provino, A. Pathak, V. Smetana, A.-V. Mudring, M. Putti, C. Federghini, V. K. Pecharsky, P. Manfrinetti, 62th conference on magnetism and magnetic materials (MMM 2017). November 6-10, Pittsburg, PA, USA, 2017.
[27] J.W. Herchenroeder, P. Manfrinetti, K.A. Gschneidner Jr, Superconductivity in metastable bcc γ-La, Phys. B+C. 135 (1985) 445–448.
[28] G.S. Anderson, S. Legvold, F.H. Spedding, Superconductivity of lanthanum and some lanthanum alloys, Phys. Rev. 109 (1958) 243–247, https://doi.org/10.1103/PhysRev.109.243.
[29] K. Yvon, W. Jeitschko, E. Parthe, LAZY PULVERIX, a computer program, for calculating X-ray and neutron diffraction powder patterns, J. Appl. Crystallogr. 10 (1977) 73–74, https://doi.org/10.1107/S0021889877012898.
[30] J. Rodriguez-Carvajal, Recent advances in magnetic structure determination by neutron powder diffraction, Phys. B 192 (1993) 55–69, https://doi.org/10.1016/0921-4526(93)90108-I.
[31] R. Blessing, An empirical correction for absorption anisotropy, Acta Crystallogr. Sect. A 51 (1995) 33–38, https://doi.org/10.1107/S0108767394005726.
[32] G. Sheldrick, SHELXT - Integrated space-group and crystal-structure determination, Acta Crystallogr. Sect. A 71 (2015) 3–8, https://doi.org/10.1107/S2053273314026370.
[33] G. Sheldrick, Crystal structure refinement with SHELXL, Acta Crystallogr. Sect. C: Struct. Chem. 71 (2015) 3–8, https://doi.org/10.1107/S2053229614024218.
[34] A. Iandelli, A. Palenzona, Zinc-rich phases of the rare-earth-zinc alloys, J. Less Common Met. 12 (1967) 333–343, https://doi.org/10.1016/0022-5088(67)90001-X.
[35] R.D. Shannon, Revised effective ionic radii and systematic studies of interatomic distances in halides and chalcogenides, Acta Crystallogr. Sect. A 32 (1976) 751–767, https://doi.org/10.1107/S0567739476001551.
[36] P. Villars, J.L.C. Daams, Atomic-environment classification of the chemical elements, J. Alloy. Compd. 197 (1993) 177–196, https://doi.org/10.1016/0925-8388(93)90041-K.
[37] K.A. Gschneidner, On the interrelationships of the physical properties of lanthanide compounds: The melting point, heat of formation and lattice parameter(s), J. Less Common Met. 17 (1969) 1–12, https://doi.org/10.1016/0022-5088(69)90031-9.
[38] P. Manfrinetti, A. Provino, K.A. Gschneidner, On the RMgSn rare earth compounds, J. Alloy. Compd. 482 (2009) 81–85, https://doi.org/10.1016/j.jallcom.2009.03.178.
[39] N.R. Werthamer, E. Helfand, P.C. Hohenberg, Temperature and purity dependence of the superconducting critical field, H_{c2}. III. Electron spin and spin-orbit effects, Phys. Rev. 147 (1966) 295–302, https://doi.org/10.1103/PhysRev.147.295.
[40] M. Couach, A. Khoder, in: R.A. Hein, T.L. Francavilla, D.H. Liebenberg (Eds.), Magnetic Susceptibility of Superconductors and Other Spin Systems, Plenum, New York, 1991, p. 35.
[41] J. Annett, Oxford, New York. Superconductivity, Superfluids and Condensates, Oxford University Press, 2004, p. 86.
[42] R. Kishore, S. Lamba, Specific heat jump in BCS superconductors, Eur. Phys. J. B 8 (1999) 161–164, https://doi.org/10.1007/s100510050678.
[43] M.L. Fornasini, P. Manfrinettib, A. Palenzonab, S.K. Dharc, R_2Sn_3 (R = La – Nd, Sm): a family of intermetallic compounds with their own triclinic structure, Z. Naturforsch. B 58 (2003) 521–527, https://doi.org/10.1515/znb-2003-0606.
[44] U. Häussermann, S. Amerioun, L. Eriksson, C.-S. Lee, G.J. Miller, The s−p bonded representatives of the prominent $BaAl_4$ structure type: a case study on structural stability of polar intermetallic network structures, J. Am. Chem. Soc. 124 (2002) 4371–4383, https://doi.org/10.1021/ja012392v.
[45] C. Zheng, R. Hoffmann, An unusual electron count and electron-deficient multi-center bonding in one class of intermetallics: the $BaAl_4$, $CaAl_2Zn_2$, $CeMg_2Si_2$ and FCC Al structures, Z. Naturforsch. B 41 (1986) 292–320, https://doi.org/10.1515/znb-1986-0304.
[46] J.K. Burdett, G.J. Miller, Fragment formalism in main-group solids: applications to aluminum boride (AlB_2), calcium aluminum silicide ($CaAl_2Si_2$), barium-aluminum ($BaAl_4$), and related materials, Chem. Mater. 2 (1990) 12–26, https://doi.org/10.1021/cm00007a004.
[47] K.S. Fries, S. Steinberg, Fermi-level characteristics of potential chalcogenide superconductors, Chem. Mater. 30 (2018) 2251–2261, https://doi.org/10.1021/acs.chemmater.7b04767.